



Identifying Young Stellar Objects in the Outer Galaxy: $l = 224^\circ$ Region in Canis Major

Marta Sewilo^{1,2}, Barbara A. Whitney^{3,4}, Bosco H. K. Yung^{5,6}, Thomas P. Robitaille⁷, Davide Elia⁸, Remy Indebetouw^{9,10}, Eugenio Schisano^{8,11}, Ryszard Szczerba^{5,6}, Agata Karska¹², Jennifer Wiseman¹³, Brian Babler⁴, Martha L. Boyer¹⁴, William J. Fischer¹⁴, Marilyn Meade⁴, Luca Olmi¹⁵, Deborah Padgett¹⁶, and Natasza Siódmiak⁵

¹Department of Astronomy, University of Maryland, College Park, MD 20742, USA; marta.m.sewilo@nasa.gov

²CRESST II and Exoplanets and Stellar Astrophysics Laboratory, NASA Goddard Space Flight Center, Greenbelt, MD 20771, USA

³Space Science Institute, 4750 Walnut St., Suite 205, Boulder, CO 80301, USA

⁴Department of Astronomy, University of Wisconsin—Madison, 475 North Charter St., Madison, WI 53706, USA

⁵Nicolaus Copernicus Astronomical Centre, PAS, Rabiańska 8, 87-100 Toruń, Poland

⁶Astronomical Observatory of the Jagiellonian University, ul. Orla 171, 30-244 Kraków, Poland

⁷Freelance Consultant, Headingley Enterprise and Arts Centre, Bennett Road Headingley, Leeds LS6 3HN, UK

⁸Istituto di Astrofisica e Planetologia Spaziali, INAF-IAPS, Via Fosso del Cavaliere 100, I-00133 Roma, Italy

⁹Department of Astronomy, University of Virginia, P.O. Box 3818, Charlottesville, VA 22903, USA

¹⁰National Radio Astronomy Observatory, 520 Edgemont Rd., Charlottesville, VA 22903, USA

¹¹Istituto di Radio Astronomia, INAF-IRA, Via Pietro Gobetti 101, I-40126, Bologna, Italy

¹²Centre for Astronomy, Faculty of Physics, Astronomy and Informatics, Nicolaus Copernicus University, Grudziądzka 5, 87-100 Toruń, Poland

¹³NASA Goddard Space Flight Center, 8800 Greenbelt Rd., Greenbelt, MD 20771, USA

¹⁴Space Telescope Science Institute, 3700 San Martin Dr., Baltimore, MD 21218, USA

¹⁵INAF, Osservatorio Astrofisico di Arcetri, Largo E. Fermi 5, I-50125 Firenze, Italy

¹⁶NASA Jet Propulsion Laboratory, California Institute of Technology, 4800 Oak Grove Dr., Pasadena, CA 91109, USA

Received 2018 August 28; revised 2018 November 27; accepted 2018 November 28; published 2019 February 1

Abstract

We study a very young star-forming region in the outer Galaxy that is the most concentrated source of outflows in the *Spitzer Space Telescope* GLIMPSE360 survey. This region, dubbed CMa-*l*224, is located in the Canis Major OB1 association. CMa-*l*224 is relatively faint in the mid-infrared, but it shines brightly at the far-infrared wavelengths as revealed by the *Herschel Space Observatory* data from the Hi-GAL survey. Using the 3.6 and 4.5 μm data from the *Spitzer*/GLIMPSE360 survey, combined with the *JHK_s* Two Micron All Sky Survey (2MASS) and the 70–500 μm *Herschel*/Hi-GAL data, we develop young stellar object (YSO) selection criteria based on color–color cuts and fitting of the YSO candidates’ spectral energy distributions with YSO 2D radiative transfer models. We identify 293 YSO candidates and estimate physical parameters for 210 sources well fit with YSO models. We select an additional 47 sources with GLIMPSE360-only photometry as “possible YSO candidates.” The vast majority of these sources are associated with high H_2 column density regions and are good targets for follow-up studies. The distribution of YSO candidates at different evolutionary stages with respect to *Herschel* filaments supports the idea that stars are formed in the filaments and become more dispersed with time. Both the supernova-induced and spontaneous star formation scenarios are plausible in the environmental context of CMa-*l*224. However, our results indicate that a spontaneous gravitational collapse of filaments is a more likely scenario. The methods developed for CMa-*l*224 can be used for larger regions in the Galactic plane where the same set of photometry is available.

Key words: infrared: stars – ISM: jets and outflows – stars: formation – stars: pre-main sequence

Supporting material: figure set, machine-readable tables

1. Introduction

Since the advent of the *Spitzer Space Telescope* (*Spitzer*; Werner et al. 2004), young stellar objects (YSOs) in the Galaxy have been studied extensively (e.g., Gutermuth et al. 2009; Povich et al. 2011; Megeath et al. 2012; Dunham et al. 2015). Most of these studies, however, have concentrated on individual, well-known star formation regions in the inner Galaxy, leaving the larger environments outside the central regions and in the outer Galaxy unstudied. However, star formation in the outer Galactic disk has increasingly been gaining attention in the past few years (e.g., Elia et al. 2013; Schisano et al. 2014; Fischer et al. 2016; Olmi et al. 2016).

The Warm *Spitzer* Exploration Science Program “GLIMPSE360: Completing the *Spitzer* Galactic Plane Survey” (3.6 and 4.5 μm ; Meade et al. 2014) is a large-scale survey covering the outer Galactic disk, enabling star formation studies with high sensitivity and angular resolution in these

relatively uncharted territories, in environments different than in the inner Galaxy (e.g., reduced metallicity at larger Galactocentric distances, lower cosmic-ray flux; Bloemen et al. 1984; Balser et al. 2011). The GLIMPSE360 survey can detect low-mass star formation throughout the Perseus spiral arm (at a distance of ~ 3.6 kpc toward $l = 225^\circ$) and higher-mass star formation beyond.

One of the most interesting regions uncovered by the GLIMPSE360 survey is located at $l \sim 224^\circ$. It contains a large concentration of sources associated with extended 4.5 μm emission that resemble the extended green objects (EGOs) identified by Cyganowski et al. (2008) in the inner Galaxy based on the images from the *Spitzer* “Galactic Legacy Infrared Mid-Plane Survey Extraordinaire” (GLIMPSE; Benjamin et al. 2003). The 4.5 μm emission is likely dominated by H_2 emission from outflow shocks, a scenario that is supported by high angular resolution SiO detections (Cyganowski et al. 2011). Maser surveys show that EGOs possess dense gas and

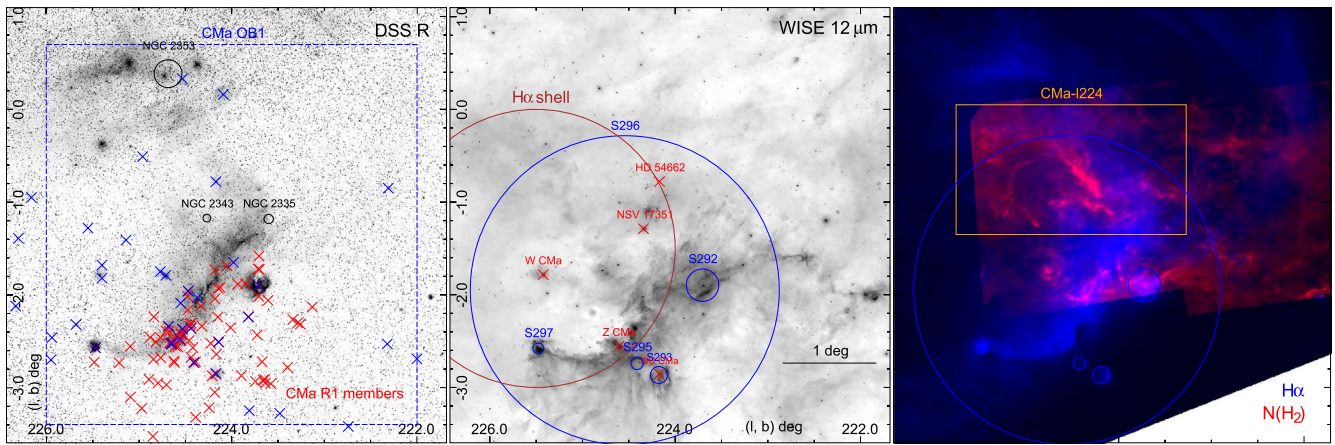


Figure 1. Digital Sky Survey (DSS) R (left), *WISE* 12 μm (middle), and combined SHASSA $\text{H}\alpha$ (“The Southern $\text{H}\alpha$ Sky Survey Atlas”; Gaustad et al. 2001) and H_2 column density (based on the *Herschel* data; Elia et al. 2013; right) images of the Canis Major (CMA) OB1 association (Ruprecht 1966; Gregorio-Hetem et al. 2009). All three images show the same area on the sky. Overlaid on the DSS R image in the left panel are the members of the CMA OB1 (Clariá, 1974b) and CMA R1 (Shevchenko et al. 1999) associations, shown as blue and red crosses, respectively. The blue box shows the boundaries of the CMA OB1 association (Ruprecht 1966). Several well-known open clusters (black circles; e.g., Dias et al. 2002; Moitinho et al. 2006; Kharchenko et al. 2013) and stars (red crosses; Gregorio-Hetem 2008 and references therein) are indicated in the left and middle panels, respectively. In the middle and right panels, the H II regions from the Sharpless (1959) catalog are shown as blue circles. The brown circle indicates the approximate position of the $\text{H}\alpha$ ring. The orange rectangle in the right panel shows the region we study in this paper, which we dubbed “CMA-I224”; it encloses the region rich in outflows (as traced by the 4.5 μm emission) and was selected based on the *Herschel* emission as described in Section 1.

outflow activity characteristic for the earliest, deeply embedded YSOs (e.g., He et al. 2012; Cyganowski et al. 2013). Thus, the region at $l \sim 224^\circ$ is the site of a very young population of protostars, actively feeding back on their surroundings.

The outflow area is located within the boundaries of the Canis Major (CMA) OB1 association ($222^\circ < l < 226^\circ$, $-3.4^\circ < b < +0.7^\circ$; see Figure 1; Ambartsumian 1949; Ruprecht 1966), $\sim 50'$ northeast from the largest H II region in the area Sh 2-296 (hereafter S296; Sharpless 1959), at a distance of ~ 1 kpc (Clariá 1974a; Shevchenko et al. 1999; Kaltcheva & Hilditch 2000). S296 is the most prominent feature in the images of the CMA OB1 association, forming a long arc of emission in the central part of the association. Another striking feature, at optical wavelengths in particular, is the H II region S292 (IC 2177)—a regularly shaped nebulosity with a dark lane across its face. S292 and nearby H II regions S293, S295, and S297 are associated with reflection nebulae (RNe; Magakian 2003) and are members of the CMA R1 association. CMA R1 is defined by a group of stars embedded in RNe, located within the boundaries of the CMA OB1 association in the galactic latitude range from -3.4° to -2.0° (van den Bergh 1966). The CMA OB1 and CMA R1 associations are physically related (Clariá 1974b).

Nineteen confirmed open clusters are located within the boundaries of CMA OB1 (e.g., Dias et al. 2002; Moitinho et al. 2006; Kharchenko et al. 2013); three of them have been studied in detail: NGC 2335, NGC 2343, and NGC 2353 (see Figure 1). These three open clusters with distances similar to that of the CMA OB1 association were suspected to be physically related to the OB1/R1 complex in early studies (e.g., Ruprecht 1966); however, the cluster ages estimated in later studies are inconsistent with this hypothesis (~ 15 to over 100 Myr versus ~ 3 Myr; e.g., Clariá 1974b; Fitzgerald et al. 1990; Lim et al. 2011; Kharchenko et al. 2013).

The optical and radio images of the CMA OB1 association reveal a large-scale ring of emission nebulosity with a diameter of $\sim 3^\circ$ centered at $(l, b) \sim (225.5, -1.5)$, defined by S296 and fainter nebulae to the north and east (see Figure 1;

Herbst & Assoua 1977). The studies on kinematics of the neutral (HI; Herbst & Assoua 1977 and references therein) and ionized ($\text{H}\alpha$ and $[\text{N II}]$; Reynolds & Ogden 1978) gas revealed that the shell is expanding. The origin of the large-scale expanding shell of ionized gas in the CMA OB1 association is still being debated. One of the hypotheses is that the shell was produced by a supernova explosion that triggered star formation in the region (Herbst & Assoua 1977; Nakano et al. 1984; Cameron et al. 1998); however, models involving strong stellar winds or an evolving H II region are not ruled out (Reynolds & Ogden 1978; Nakano et al. 1984).

CMA OB1 was covered by the $^{13}\text{CO}(J=1-0)$ survey of the Monoceros and Canis Major region ($\sim 560 \text{ deg}^2$; $208^\circ \leq l \leq 230^\circ$, $-20^\circ \leq b \leq 10^\circ$) with the NANTEN millimeter-wave telescope at 2.6 resolution (Kim et al. 2004). Kim et al. (2004) detected a giant molecular cloud complex associated with the CMA OB1 association and comparable in size to S296. Kim et al. (2004) identified 115 CO clouds in the survey area; 11 are within the boundaries of the CMA OB1 association. The higher-resolution ($43''$) $^{12}\text{CO}(J=1-0)$ survey with the SEST telescope was conducted toward *IRAS* sources with colors of star-forming regions in the outer Galaxy ($b \leq 10^\circ$ and $85^\circ < l < 280^\circ$) by Wouterloot & Brand (1989), detecting 18 CO clouds in the CMA OB1 association.

The CMA-I224 outflow region overlaps with the first outer Galaxy region ($216.5^\circ \lesssim l \lesssim 225.5^\circ$, $-2^\circ \lesssim b \lesssim 0^\circ$) studied using the *Herschel Space Observatory* (*Herschel*; Pilbratt et al. 2010) data from the Open Time Key Project “*Herschel* infrared Galactic Plane Survey” (Hi-GAL; Molinari et al. 2010). This Hi-GAL study by Elia et al. (2013) based on the PACS 70 and 160 μm (Poglitsch et al. 2010) and SPIRE 250, 350, and 500 μm data (Griffin et al. 2010), combined with the *WISE* 22 μm photometry, constructed a catalog of *Herschel* compact sources (cores and clumps) that they classify as protostellar (with a detection at 70 μm and/or at 22 and 160 μm ; 255 sources) and starless (688). They found that most of the protostellar sources are in the early accretion phase, while for prestellar sources the accretion has not started yet. The

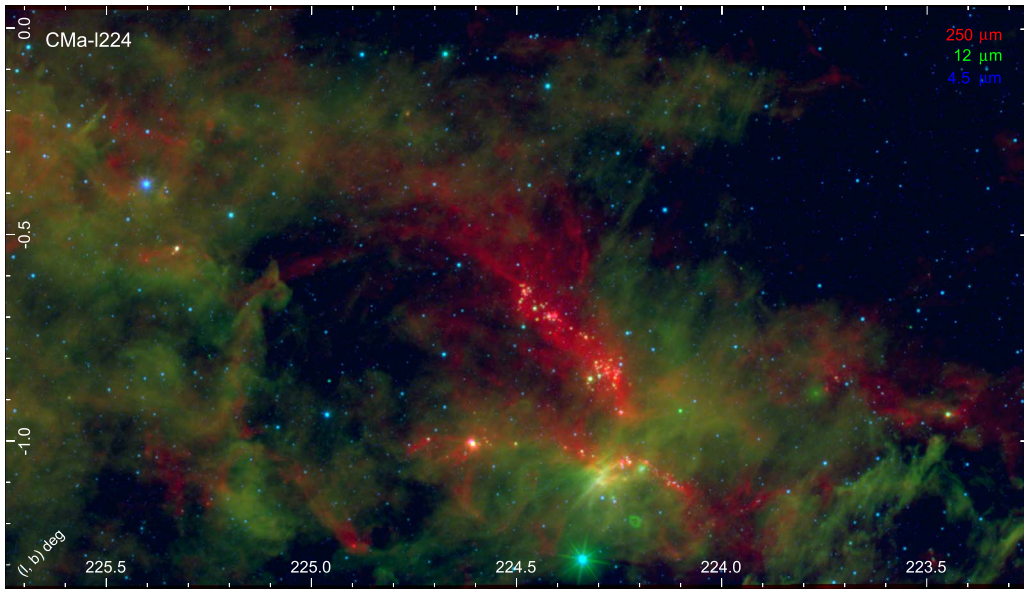


Figure 2. Three-color composite image combining the *Herschel*/Hi-GAL SPIRE 250 μm (red), *WISE* 12 μm (green), and *Spitzer*/GLIMPSE360 IRAC 4.5 μm (blue) mosaics. The image shows a region indicated with the orange rectangle in the right panel of Figure 1.

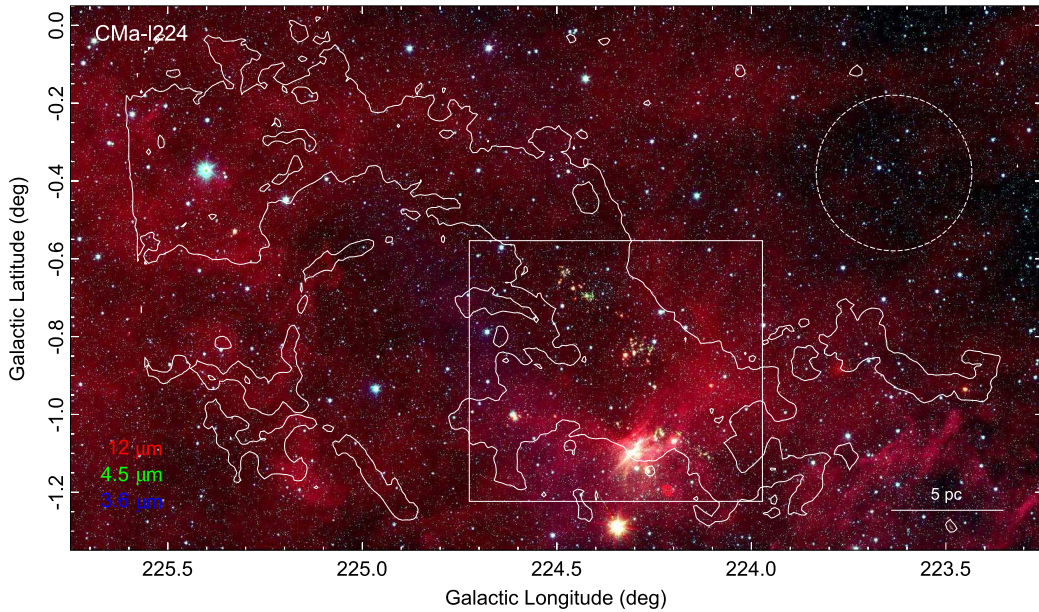


Figure 3. Three-color composite image of CMA-*l*224 combining the *WISE* 12 μm (red), GLIMPSE360 4.5 μm (green), and GLIMPSE360 3.6 μm (blue) images. The region rich in outflows (traced by 4.5 μm emission) is located in the central part of the image. The white box indicates the area shown in Figure 4; it is very bright at *Herschel* wavelengths, indicating the earliest stages of star formation. The white contour corresponds to the H_2 column density of $4 \times 10^{21} \text{cm}^{-2}$. The region within the white circle represents the background emission in our analysis. The scale bar at the lower right corresponds to 5 pc assuming a distance of 1 kpc.

temperature and H_2 column density maps derived using the 160–500 μm data reveal a variety of conditions, with star formation preferentially distributed along filamentary structures. The filaments were identified in follow-up work by Schisano et al. (2014) using the H_2 column density map. The outflow region includes areas characterized by the lowest temperatures and the highest H_2 column densities in the entire region studied by Elia et al. (2013) and Schisano et al. (2014).

The area studied in this work was selected based on the H_2 column density map from Elia et al. (2013). It encloses a high column density ring-like structure (as traced by the $4 \times 10^{21} \text{cm}^{-2}$ contour); the western side of this structure is

formed by the two brightest *Herschel* filaments in the region that coincide with the outflows (Figures 2–4). The size of the selected region is 2.5×1.4 , with the center at $(l, b) = (224.5, -0.65)$; see Figures 1–3. We refer to this region as “CMA-*l*224” throughout the paper.

The goal of this paper is to identify YSO candidates in CMA-*l*224 using the high-sensitivity GLIMPSE360 3.6 and 4.5 μm data combined with ancillary catalogs and images. We estimate the physical parameters of the YSO candidates and study their correlations with the dust and gas tracers. The methods developed for this relatively small region can be applied to the larger areas in the outer Galactic plane where *Spitzer*

Table 1
Photometric Data Used in This Study and the Angular Resolutions of the Surveys

Wavelength (μm)	Instrument	Survey	FWHM (arcsec)
1.2	2MASS	All-Sky 2MASS	2–3 ^a
1.6	2MASS	All-Sky 2MASS	2–3
2.2	2MASS	All-Sky 2MASS	2–3
3.6	<i>Spitzer</i> IRAC	GLIMPSE360	1.7
4.5	<i>Spitzer</i> IRAC	GLIMPSE360	1.7
8.3	<i>MSX</i> SPIRIT III	<i>MSX</i>	~ 20
9	<i>AKARI</i> IRC	All-Sky Survey	5.5
12	<i>WISE</i>	All-Sky <i>WISE</i> /NEOWISE	6.5
12.1	<i>MSX</i> SPIRIT III	<i>MSX</i>	~ 20
14.7	<i>MSX</i> SPIRIT III	<i>MSX</i>	~ 20
18	<i>AKARI</i> IRC	All-Sky Survey	5.7
21.3	<i>MSX</i> SPIRIT III	<i>MSX</i>	~ 20
22	<i>WISE</i>	All-Sky <i>WISE</i> /NEOWISE	12
70	<i>Herschel</i> PACS	Hi-GAL ^b	$\sim 10^c$
160	<i>Herschel</i> PACS	Hi-GAL	12 ^c
250	<i>Herschel</i> SPIRE	Hi-GAL	18 ^c
350	<i>Herschel</i> SPIRE	Hi-GAL	25 ^c
500	<i>Herschel</i> SPIRE	Hi-GAL	36 ^c

Notes.

^a Depending on the atmospheric seeing.

^b The Hi-GAL source list from Elia et al. (2013).

^c Molinari et al. (2016).

photometry at longer wavelengths is not available, making the methods developed for the nearby molecular clouds unsuitable (e.g., Gutermuth et al. 2009; Dunham et al. 2015). These new methods enable systematic studies of the outer Galaxy, covering a range of environments and star formation activities, to uncover and characterize a relatively unstudied population of intermediate- and low-mass YSOs and study the impact of the environment on the star formation process (e.g., outer versus inner Galaxy, arm versus interarm regions, positions in the Galaxy with different chemical abundances, etc.).

In Sections 2 and 3, we describe the catalogs and images used in the analysis and the catalog matching, respectively. The method of distance determination is described in Section 4. The initial YSO selection criteria are provided in Section 5. Sections 6–9 provide details on the subsequent analysis that selected the most reliable YSO candidates. We compare our list of YSO candidates to the catalog of previously known *WISE* YSO candidates in Section 10. In Sections 11 and 12, we compare the spatial distribution of YSO candidates to the dust and gas tracers. We discuss possible star formation scenarios in the region in Section 13. The summary and conclusions are provided in Section 14.

2. The Data

Our study is mainly based on the catalogs and images from the GLIMPSE360 survey (PI B. Whitney). GLIMPSE360 observed the outer Galactic plane at 3.6 and 4.5 μm with the Infrared Array Camera (IRAC; Fazio et al. 2004), covering a longitude range from 65° to 265°, excluding regions covered by smaller surveys (SMOG: $l = 102^\circ\text{--}109^\circ$, PI S. Carey; Cygnus-X: $l = 76^\circ\text{--}82^\circ$, Beerer et al. 2010). The GLIMPSE360 data products are described in the data delivery document available at the NASA/IPAC Infrared Science Archive (Meade et al. 2014). We complemented the GLIMPSE360 data with the ancillary

data from previous near- to far-infrared (IR) surveys (see Section 2.2). Table 1 includes a list of photometric catalogs used in our analysis, together with the angular resolutions of the observations.

2.1. Primary Data Set: *Spitzer* GLIMPSE360

The GLIMPSE360 data products include a highly reliable IRAC Point Source Catalog and a more complete IRAC Point Source Archive (see Meade et al. 2014 for details). In our analysis, we use the IRAC Archive for completeness in both the number of sources and the flux measurements at each wavelength. The sources included in the Archive fulfill less stringent criteria than those included in the Catalog; however, these criteria were developed to ensure that each source is a legitimate astronomical source and that the fluxes reported for the IRAC bands are of high quality. The *Spitzer* GLIMPSE360 data are matched to the near-IR (JHK_s) data from the Two Micron All Sky Survey (2MASS; Skrutskie et al. 2006); 2MASS photometry is an integral part of the GLIMPSE360 Catalog and Archive.

About 212,000 GLIMPSE360 sources are located in CMA-1224 (see Table 2). The lower and upper sensitivity limits in the 3.6 μm band are 0.021 mJy (17.8 mag) and 1100 mJy (6.0 mag), respectively. In the 4.5 μm band, the lower and upper sensitivity limits are 0.022 mJy (17.3 mag) and 1100 mJy (5.5 mag), respectively (Meade et al. 2014). The minimum signal-to-noise ratio (S/N) is 5 in both bands. Figure 5 shows example color–color and color–magnitude diagrams (CCDs and CMDs) using the *Spitzer* and 2MASS data.

2.2. Complementary Mid-IR to Submillimeter Data

We supplement the *Spitzer* GLIMPSE360 data with the longer-wavelength *WISE*/NEOWISE (Section 2.2.1), *AKARI* (Section 2.2.2), *Midcourse Space Experiment* (*MSX*; Section 2.2.3), and *Herschel* (Section 2.2.4) data (see Table 1). The longer-wavelength data probe the embedded population of YSOs more deeply.

2.2.1. AllWISE

We supplement the GLIMPSE360 data with the 12 and 22 μm catalogs and images from the AllWISE program. A longer-wavelength photometry improves the YSO identification, allowing better separation between protostars and more evolved YSOs. The AllWISE program combines the data from the *Wide-field Infrared Survey Explorer* (*WISE*; Wright et al. 2010) cryogenic and NEOWISE (Mainzer et al. 2011) post-cryogenic survey phases. The AllWISE products have improved photometric sensitivity and accuracy, as well as astrometric precision compared to the original *WISE* All-Sky Data Release.

The sensitivity of the *WISE*/NEOWISE survey is much lower than that of the GLIMPSE360 survey, and thus the combination of GLIMPSE360 and AllWISE bands will miss sources that were only detected at *Spitzer* bands. We do not use *WISE* 3.4 and 4.6 μm filters that are similar to GLIMPSE360/IRAC 3.6 and 4.5 μm filters since the sensitivity limits of the GLIMPSE360 survey are much deeper and the saturation limits are higher. GLIMPSE360 also provides three times better spatial resolution (2" versus *WISE* 6").

Koenig & Leisawitz (2014) investigate the performance of the AllWISE catalog in the Galactic plane by analyzing the data

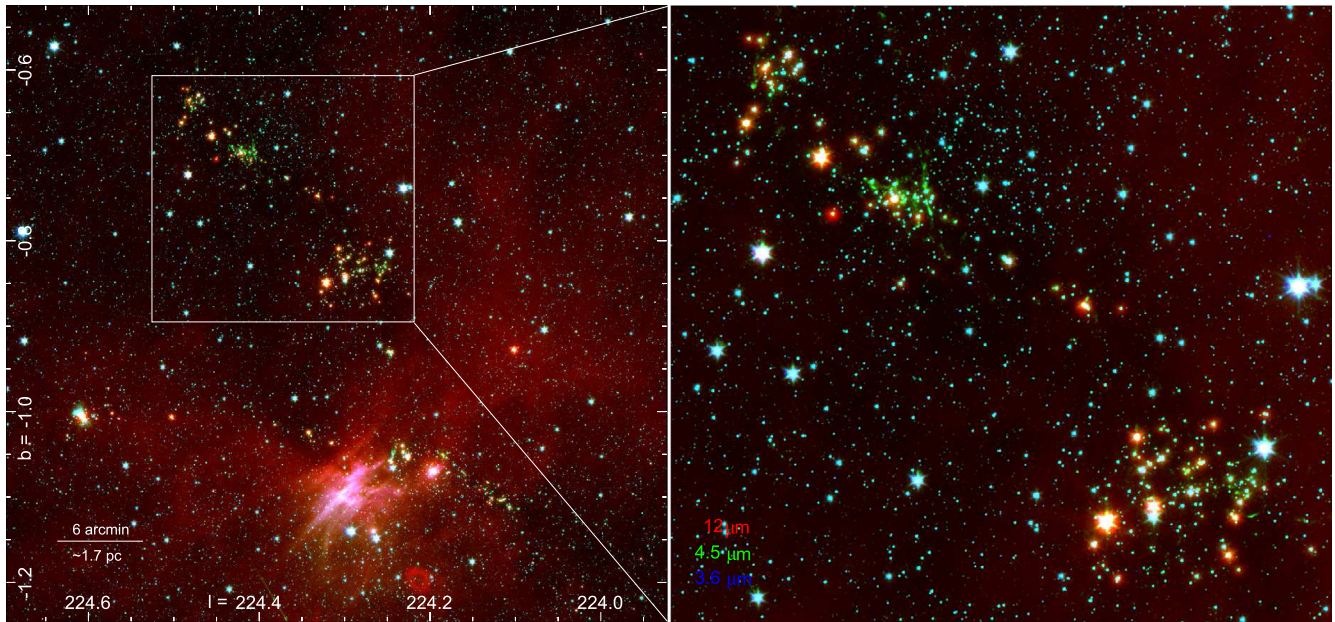


Figure 4. Left: image showing the region indicated with a white box in Figure 3 in the same combination of colors. This area harbors sources with outflows (traced by enhanced $4.5\ \mu\text{m}$ emission). The source at $(l, b) \sim (224.6, -1^\circ)$ is the reflection nebula Gy 3–7 associated with the embedded cluster and the high-luminosity IRAS source IRAS 07069–1045 (Gy 3–7 #6; Tapia et al. 1997). Right: zoom-in on the area enclosed in the white box in the left panel.

for the W3 and W5 giant molecular clouds and part of the W4 region. They found that in *WISE* Band 3 ($12\ \mu\text{m}$) and Band 4 ($22\ \mu\text{m}$), the AllWISE source extraction pipeline retrieves only 50%–60% and 75% of sources seen in the *WISE* images, respectively. They also found that the vast majority of the AllWISE 12 and $22\ \mu\text{m}$ catalog sources with an S/N larger than 5 are likely spurious detections, especially in the high-sky background regions; they likely represent upper limit measurements of the nebular background.

In this work, we use the profile fitting photometry—columns $w?mpro$ and $w?msigpro$ (magnitude and magnitude uncertainty, respectively) in the online AllWISE catalog. The AllWISE catalog includes the photometric quality flag (ph_qual column), which provides information on the quality of the profile-fit photometry measurement in each band based on the S/N of the measurement. The photometric quality flag “U” indicates that the quoted magnitude is computed from a 2σ brightness upper limit. For valid flux measurements, ph_qual is “A,” “B,” or “C,” depending on the S/N ($w?snr$ column): $w?snr \geq 10$, $3 < w?snr < 10$, $2 < w?snr < 3$, respectively. Out of 80,171 AllWISE sources (74,726 point sources: extended source flag $ext_flg = 0$) in CMa–l224, $\sim 74\%$ ($\sim 75\%$) have $12\ \mu\text{m}$ photometry and $\sim 90\%$ ($\sim 91\%$) have $22\ \mu\text{m}$ photometry flagged as an upper limit. Only 6310 AllWISE sources (5352 point sources) have valid 12 and $22\ \mu\text{m}$ photometry.

We use the zero magnitude flux of 31.674 and 8.363 Jy (Jarrett et al. 2011) to calculate, respectively, the 12 and $22\ \mu\text{m}$ fluxes from magnitudes.

2.2.2. AKARI

To provide additional longer-wavelength photometry for GLIMPSE360 sources in CMa–l224, we use the data from the *Infrared Astronomical Satellite AKARI* Infrared Camera (IRC) All-Sky Survey (Murakami et al. 2007; Onaka et al. 2007; Ishihara et al. 2010). The *AKARI* IRC catalog (version 1.0) provides photometry in two mid-IR bands: MIR-S ($9\ \mu\text{m}$) and MIR-L ($18\ \mu\text{m}$). The spatial resolutions (FWHM) in the 9 and

$18\ \mu\text{m}$ bands are $\sim 5''.5$ and $\sim 5''.7$, respectively. For an S/N of ~ 5 , the detection limits in the MIR-S and MIR-L bands are about 0.05 and 0.09 Jy, respectively (Kataza et al. 2010). Since the GLIMPSE360 observations are much deeper, we expect to find *AKARI* counterparts only for the brightest GLIMPSE360 sources. There are 102 *AKARI* IRC point sources in the CMa–l224 region.

The zero-magnitude fluxes are 56.262 and 12.001 Jy for the 9 and $18\ \mu\text{m}$ bands, respectively (Tanabé et al. 2008).

2.2.3. MSX

Our analysis includes the data from The *MSX* Point Source Catalog (Egan et al. 2003; $\sim 20''$ resolution). We use the data from the broad spectral bands: A ($8.28\ \mu\text{m}$), C ($12.13\ \mu\text{m}$), D ($14.65\ \mu\text{m}$), and E ($21.3\ \mu\text{m}$). The survey sensitivity in Band (A, C, D, E) is (0.1–0.2, 1.1–3.1, 0.9–2, 2–6) Jy (early–late in the mission; Egan et al. 2003). As for the *AKARI* data, due to much lower sensitivity of the *MSX* survey than the GLIMPSE360 survey, only a small fraction of *Spitzer* sources have *MSX* counterparts. There are 78 *MSX* sources in CMa–l224.

The zero-magnitude fluxes are (58.49, 26.51, 18.29, 8.80) Jy for (A, C, D, E) bands (Egan et al. 2003).

2.2.4. Herschel Hi-GAL

We use the catalog of *Herschel* Hi-GAL sources provided by Elia et al. (2013) (see Section 1). Their full catalog includes the PACS 70 and $160\ \mu\text{m}$ and SPIRE 250, 350, and $500\ \mu\text{m}$ photometry for high-reliability *Herschel* compact sources eligible for graybody fit from the $\sim 18\ \text{deg}^2$ area in the third Galactic quadrant. Each source has valid fluxes in at least three consecutive bands and spectral energy distributions (SEDs) not showing dips and not peaking at $500\ \mu\text{m}$. The Elia et al. (2013) catalog provides not only the 70– $500\ \mu\text{m}$ photometry but also kinematic distances (estimated based on the CO data), physical properties of the sources (source sizes, masses, temperatures,

Table 2
Source Statistics for CMA-1224

Source Type	No. of Sources
<i>Spitzer</i> /GLIMPSE360 sources	211,900
AllWISE sources	80,171 (74,726) ^a
<i>AKARI</i> /IRS sources	102
<i>MSX</i> Point Source Catalog sources	78
<i>Herschel</i> /Hi-GAL sources (Elia et al. 2013) ^b	273
<i>Herschel</i> /Hi-GAL sources (Full) ^b	787
<hr/>	
GLIMPSE360 sources with valid 3.6 and 4.5 μm photometry	202,575
AllWISE sources with valid 12 μm photometry ^c	21,255 (18,919) ^a
AllWISE sources with valid 22 μm photometry ^c	8,200 (7064) ^a
AllWISE sources with valid 12 and 22 μm photometry ^c	6310 (5352) ^a
<i>Herschel</i> /Hi-GAL sources (Elia et al. 2013) with valid 70 μm flux	64
<i>Herschel</i> /Hi-GAL sources (Full) with valid 70 μm flux	113
<hr/>	
Matching Results ^d	
GLIMPSE360 (3.6 and 4.5 μm) with AllWISE 12 μm matches	10,557/27,646 ^e
GLIMPSE360 (3.6 and 4.5 μm) with AllWISE 22 μm matches	2335/37,862 ^e
GLIMPSE360 (3.6 and 4.5 μm) with AllWISE 12 and 22 μm matches	1878/26,371 ^e
GLIMPSE360 (3.6 and 4.5 μm) with <i>AKARI</i> matches	58
GLIMPSE360 (3.6 and 4.5 μm) with <i>MSX</i> matches	26
GLIMPSE360 (3.6 and 4.5 μm) with <i>Herschel</i> matches (Elia et al. 2013) ^b	72 (40) ^f
GLIMPSE360 (3.6 and 4.5 μm) with <i>Herschel</i> matches (Full)	206 (75) ^g

Notes.

^a The number in parentheses corresponds to point sources (*ext_flg* = 0).

^b Based on the Hi-GAL catalog from Elia et al. (2013). In order to be included in the catalog, a source had to be detected in at least three consecutive bands.

^c AllWISE catalog sources with the *ph_qual* of “A,” “B,” or “C” (i.e., no upper limits) in a corresponding band.

^d The matching radii between the GLIMPSE360 catalog and AllWISE, *AKARI*, *MSX*, *Herschel*/E10, and *Herschel*/Full are 1”, 1”, 1”/3, 5”, and 5”, respectively. All the constraints described in Section 3 are applied.

^e The numbers represent the number of sources with valid data points (left) and upper limits (right) at a corresponding wavelength(s).

^f The number in parentheses corresponds to sources with valid 70 μm flux. Out of 72 sources, 26 are SPIRE-only and are not used in the analysis.

^g The number in parentheses corresponds to sources with valid 70 μm flux. Out of 206 sources, 111 are SPIRE-only and are not used in the analysis.

and bolometric luminosities), and their classification. Two hundred and seventy-three *Herschel* sources from the Elia et al. (2013) catalog are located in CMA-1224: 29 unbound, 171 pre-stellar, and 73 protostellar cores (see Figure 6). The *Herschel* cores/clumps are classified as protostellar if they are detected at the PACS 70 μm and/or *WISE* 22 μm and at the PACS 160 μm bands.

In addition to the Elia et al. (2013) catalog (their Table 3), we also use the more complete catalog that was used to select these sources (unpublished; D. Elia 2018, private communication) and refer to it as the “Full *Herschel* catalog.” Although the Elia et al. (2013) catalog is a subset of the Full *Herschel* catalog, we consider them separately since the sources from the Elia et al. (2013) catalog were analyzed in detail and classified as described above, while the Full *Herschel* catalog includes all the sources extracted from the images that fulfill a set of the quality

criteria (all five-band photometry is included regardless of the completeness/regularity of the SED). We are able to identify unreliable photometry in the subsequent analysis. There are 787 sources from the Full *Herschel* catalog in CMA-1224.

In our analysis, we use the H₂ column density and temperature images derived by Elia et al. (2013) through a pixel-to-pixel graybody fit using the Hi-GAL 160–500 μm images; they represent the properties of the cold component of dust.

The *Herschel* PACS and SPIRE images from the Hi-GAL survey have been downloaded from the *Herschel Science Archive* (Proposal ID: OT1_smolinar_5).

2.3. The CO Data

In our analysis, we determine kinematic distances to the GLIMPSE360 sources using the NANTEN ¹²CO ($J = 1-0$) Galactic Plane Survey data (Mizuno & Fukui 2004) presented by Elia et al. (2013) for their survey area (see Section 1). The spatial resolution of the survey is 2.6”, significantly lower than the GLIMPSE360 resolution ($\sim 2''$). The spectra for $|b| \leq 0.5^\circ$ were obtained with a grid spacing of 4”. The CMA-1224 is covered in full by this survey.

3. The Catalog Matching

We positionally cross-matched the *Spitzer*/GLIMPSE360 catalog (already matched to 2MASS) with the AllWISE, *AKARI*, *MSX*, and Hi-GAL catalogs to provide longer-wavelength data that, in combination with near- and mid-IR data, would improve the YSO identification process, including the color-color/color-magnitude selection and the SED fitting. As a result of the much higher sensitivity of the GLIMPSE360 survey in comparison to other currently available surveys, only a small fraction of GLIMPSE360 sources have matches in other catalogs (see Table 2).

AllWISE: To match the GLIMPSE360 catalog with the AllWISE catalog, we adopted a matching radius of 1” and selected the closest matches. We found 80,171 matches; we used the quality flags provided in the AllWISE catalog to exclude unreliable sources. In our color-color/color-magnitude YSO selection process, we use the 12 and 22 μm (w_3 and w_4) photometry with a flag *ph_qual* of “A” or “B,” excluding low-S/N photometry and upper limits. The 12 and 22 μm flux upper limits will be used for the SED fitting if both the w_1 and w_2 fluxes have an S/N larger than or equal to 10 (*ph_qual* = “A”). We remove fluxes flagged as likely spurious detections: Diffraction spikes (*cc_flag* = “D”), Persistences (“P”), Halos (“H”), and Optical ghosts (“O”), and those flagged as extended sources with *ext_flg* > 1.

Koenig & Leisawitz (2014) found that the S/N (w_3snr) and profile-fit reduced chi-squared (w_3rchi2) parameters have the strongest discriminatory effect in suppressing spurious source contamination in *WISE* Bands 3 and 4. However, the cuts in the w_3snr versus w_3rchi2 space designed to remove spurious sources from the catalog also remove a large number of real sources from Bands 3 and 4. To increase the rate of the real source retrieval in Band 3 (up to $\sim 60\%$), Koenig & Leisawitz (2014) introduced additional criteria to recover the low-S/N sources. For Band 3, Koenig & Leisawitz (2014) proposed the following set of criteria to remove the vast majority of spurious 12 μm sources from the AllWISE catalog: $w_3snr \geq 5$ and $[(w_3rchi2 < (w_3snr - 8)/8) \text{ or } (0.45 < w_3rchi2 < 1.15)]$.

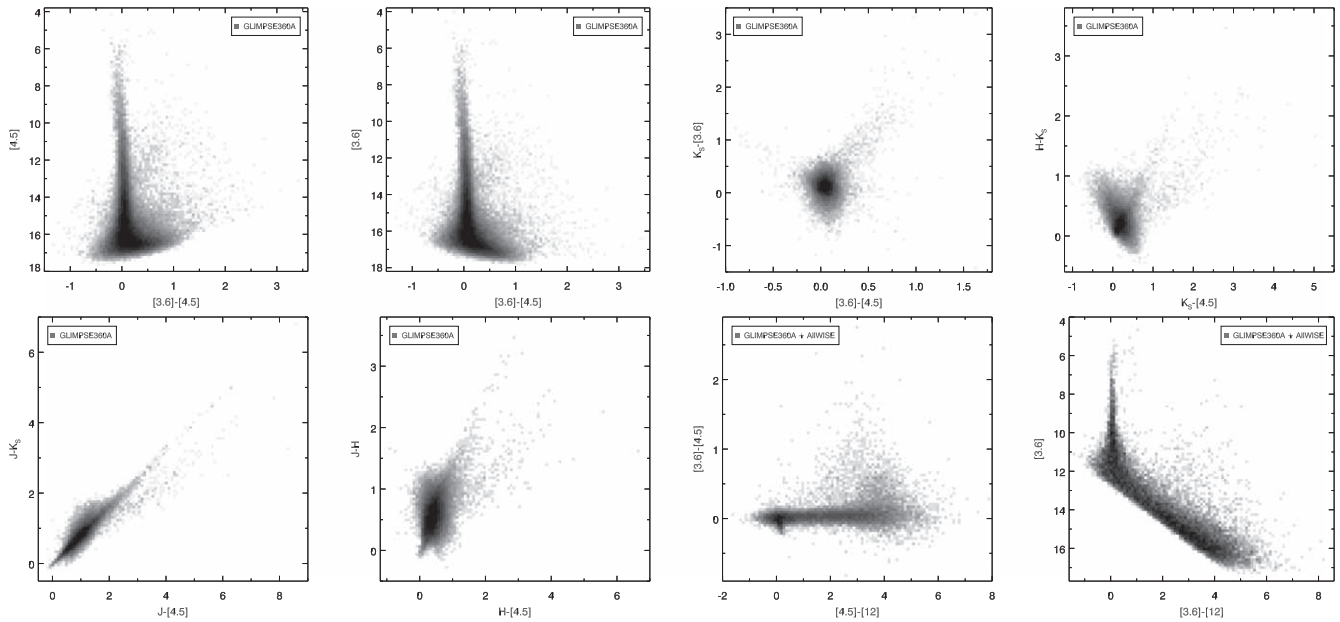


Figure 5. Example CMDs and CCDs showing the distribution of all the GLIMPSE360 IRAC Archive (GLIMPSE360A) sources with flux measurements at both 3.6 and 4.5 μm ([3.6] vs. [3.6]–[4.5] and [4.5] vs. [3.6]–[4.5]), and the distribution of the GLIMPSE360 sources with valid photometry in both *Spitzer* bands with 2MASS and/or AllWISE 12 μm matches (the remaining plots). The data are displayed as Hess diagrams; the gray scale indicates the source density in logarithmic scale (the source density range is different in each plot). The distribution of the combined catalog sources shown in these plots is compared in Section 5 to the distribution of the YSO and non-YSO sources from the literature and YSO models to develop the YSO selection criteria for CMA–I224 (see also Figures 9–13).

For *WISE* Band 4, the criteria are non-null $w4sigmpro$ (i.e., ph_qual of “A,” “B,” or “C”) and $w4rchi2 < (2 \times w4snr - 20)/10$. Only 8% of all AllWISE sources with valid fluxes in CMA–I224 fulfill these criteria in Band 3, and $\sim 0.2\%$ in Band 4. We do not apply these criteria since they remove a large fraction of real sources. We will identify spurious AllWISE detections during the visual inspection.

AKARI: To search for counterparts to GLIMPSE360 sources in the *AKARI* catalog, we used a matching radius of $1''$, which roughly corresponds to the mean *AKARI* survey’s positional accuracy (Kataza et al. 2010). We found 60 matches; 58 out of 60 GLIMPSE360 sources with *AKARI* matches have both 3.6 and 4.5 μm valid fluxes. Out of these 58 sources, 91% have a valid 9 μm flux, 22% have a valid 18 μm flux, and only 14% have valid 9 and 18 μm fluxes.

MSX: We inspected the flux quality flags (q) and selected fluxes with $q = 4$ (excellent), 3 (good), and 2 (fair/poor, $\sim 15\%$; $S/N > 5$). The positional uncertainty estimated for sources with $q \geq 2$ in A band (q_a) is $\sim 1''.3$.¹⁷ Therefore, we used the matching radius of $1''.3$ to search for counterparts of the GLIMPSE360 sources in the *MSX* catalog. For sources with fluxes at both 3.6 and 4.5 μm bands, we found (26, 3, 1, 1) matches in (A, C, D, E) band.

Hi-GAL (Elia et al. 2013): We matched the GLIMPSE360 catalog to the Elia et al. (2013) catalog and the Full *Herschel* catalog (see Section 2.2.4) using a matching radius of $5''$. There is a significant difference in angular resolutions between the *Spitzer* and *Herschel* bands, the SPIRE bands (250–500 μm) in particular (see Table 1); thus, the matching radius we selected is very conservative. However, we do not expect sources detected with *Spitzer* to be detected with SPIRE but not with PACS. Thus, we selected the matching radius based on the highest-resolution *Herschel* PACS band, i.e., 70 μm ($\sim 5''$).

We found 72 (206) matches for the GLIMPSE360 sources in the Elia et al. (2013) (Full *Herschel*) catalog, with 40 out of 72 (75 out of 206) having a valid 70 μm flux. There are 26 out of 72 (111 out of 206) SPIRE-only sources in the Elia et al. (2013) (Full *Herschel*) catalog, which will not be used in our analysis.

The matching results are summarized in Table 2. We verify the validity of the matches during the visual inspection of the images of preselected YSO candidates.

4. Distance Determination

As the volume density in the outer Galaxy is lower, there is less line-of-sight confusion, and it is easier to associate IR emission with molecular clouds identified in spectral line surveys than in the inner Galaxy. The kinematic distances to these objects are more reliable, as there is no distance ambiguity for lines of sight in quadrants II and III. The distance to YSOs can be estimated by association with either CO emission or HI self-absorption from the cold HI envelopes of molecular clouds. Since the CO data at relatively high resolution are available for the region we study, we will use the CO emission for distance determination.

We determine kinematic distances to *Spitzer* sources by associating them with CO clumps using the technique described in detail in Elia et al. (2013). They used the ^{12}CO ($J = 1-0$) data from the NANTEN CO Galactic Plane Survey (Mizuno & Fukui 2004; improved with respect to the original NANTEN survey mentioned earlier, Kim et al. 2004) to search for spatially and kinematically coherent overdense structures that they call “CO clumps.” For the cloud decomposition, they used the CLUMPFIND (Williams et al. 1994) decomposition algorithm in the CLOUDPROPS package (Rosolowsky & Leroy 2006, 2011). This analysis provides morphological and physical properties of the clumps, e.g., velocity dispersion, distance, radius, mass, virial mass, and luminosity. Elia et al.

¹⁷ https://irsa.ipac.caltech.edu/data/MSX/docs/msxpsc2.3_explguide.pdf

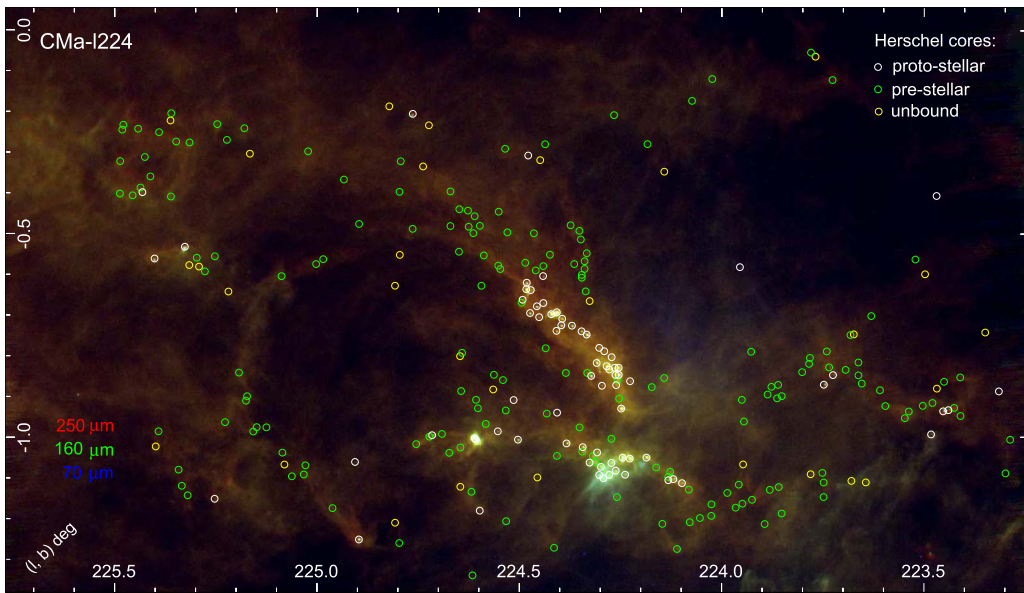


Figure 6. Three-color image combining the *Herschel* SPIRE 250 μm (red), PACS 160 μm (green), and PACS 70 μm (blue) mosaics. The white, green, and yellow circles indicate *Herschel* protostellar, starless, and unbound cores from Elia et al. (2013), respectively.

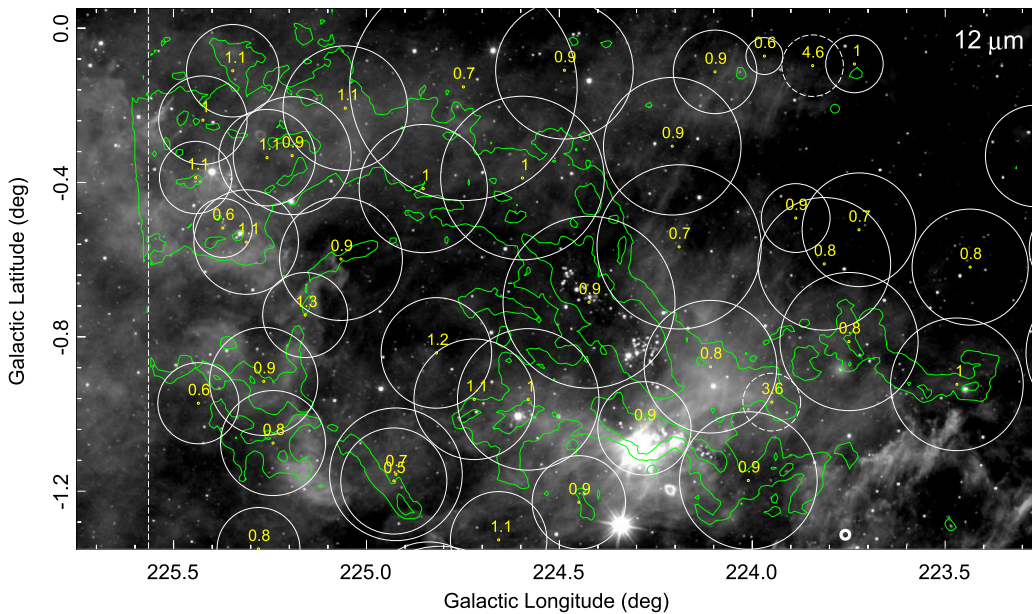


Figure 7. *WISE* 12 μm image with the positions and sizes of the CO clumps from the Elia et al. (2013) catalog indicated with white circles. The yellow labels inside the circles provide the clumps' kinematic distances in kpc. Two clumps with distances larger than 3 kpc are shown as white dashed circles. The H_2 column density contour levels are $(4, 8) \times 10^{21} \text{cm}^{-2}$. The white dashed vertical line shows the extent of the CO map.

(2013) estimated heliocentric distances to CO clumps using the rotation curve of Brunthaler et al. (2011; $R_0 = 8.3 \text{ kpc}$, $\Theta_0 = 239 \text{ km s}^{-1}$).

In the CO line of sight containing the *Spitzer* source, we consider the spectral channels assigned by CLOUDPROPS/CLUMPFIND to one or more clumps and associate with the source the distance of the clump (if any) having the closest centroid (see Figure 7). The advantages of such a strategy are discussed in Elia et al. (2013).

We assigned distances to $\sim 62\%$ of all *Spitzer* sources in CMA-I224; the distribution of distances is shown in Figure 8. About 99% of sources have distances between 0.5 and 1.3 kpc,

with a median distance of 0.92 kpc. This result is consistent with the previous distance determinations based on the photometric and spectroscopic data for OB stars in the CMA OB1 region (e.g., Clariá 1974b; Kaltcheva & Hilditch 2000), based on the early-type stars in CMA R1 (Shevchenko et al. 1999), or by comparing the observed density of foreground stars detected by 2MASS with the prediction of galactic models (Lombardi et al. 2011).

A small fraction of sources at distances larger than 3 kpc are likely associated with the Perseus spiral arm. These sources are associated with two small CO molecular clumps at $(l, b) \sim (223^\circ 9, -0^\circ 9)$ and $(223^\circ 8, -0^\circ 1)$; see Figure 7.

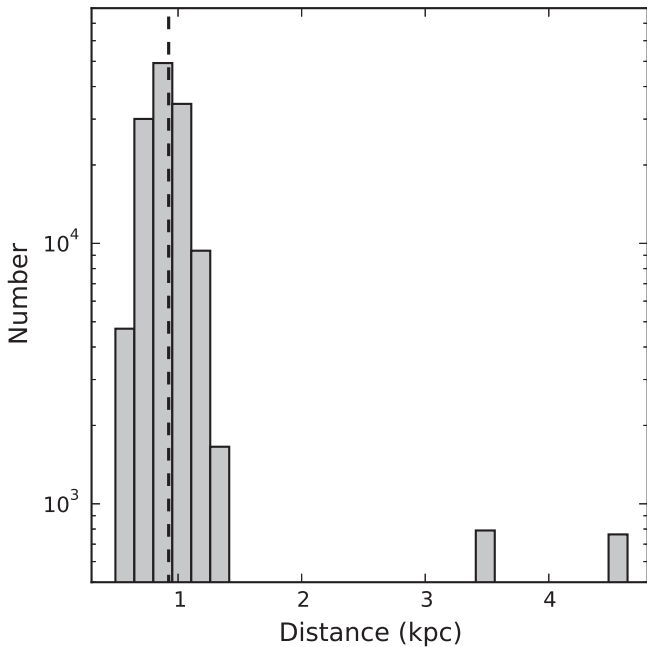


Figure 8. Distribution of kinematic distances estimated using the CO data as described in Section 4. The dashed vertical line shows a median distance of 0.92 kpc calculated using distances < 2 kpc.

5. Initial Selection of YSO Candidates

Our general strategy on selecting YSO candidates based on the 2MASS and *Spitzer* data is to first identify IR-excess sources and then apply a series of filters to remove various populations of contaminating sources. These include unresolved extragalactic objects detected in the outer Galactic plane in the deep GLIMPSE360 survey, unresolved planetary nebulae (PNe), and evolved stars. The subsequent analysis includes the SED fitting with YSO models and the visual inspection of multiwavelength images.

We identify regions in the CCD and CMD space that should be occupied predominantly by YSOs by comparing the distribution of the GLIMPSE360 catalog sources in the CCDs and CMDs to the distribution of non-YSOs from the literature (evolved stars, AGNs, and normal galaxies; Kimeswenger 2001; Urquhart et al. 2009; Kochanek et al. 2012; Reiter et al. 2015), previously identified Galactic YSOs (Fang et al. 2013) and YSO candidates (Megeath et al. 2012; Dunham et al. 2015), as well as 2D YSO radiative transfer models (Robitaille et al. 2006). All the catalogs from the literature are described in Appendix A. We assume the Flaherty et al. (2007) interstellar extinction law for the *Spitzer* IRAC bands based on the data for five nearby star-forming regions. The estimated extinction law for *WISE* bands comes from Koenig & Leisawitz (2014).

Out of 211,900 *Spitzer* GLIMPSE360 catalog sources in CMA-1224, 128,317 ($\sim 60.6\%$) do not have counterparts in any other catalog used in this paper within the selected matching radii. With only one or two valid fluxes, these sources will not fulfill any of the YSO selection criteria described below and thus are removed from the analysis. A subset of these sources with both 3.6 and 4.5 μm catalog data (119,352) and additional *Spitzer* sources that have AllWISE matches but no valid 12 and 22 μm photometry (not in the catalog or of poor quality and removed) and no matches in other catalogs are discussed separately in Section 9. Here we analyze all the sources with

valid fluxes in at least three shorter-wavelength bands, i.e., excluding *Herschel* data.

5.1. Interstellar Extinction toward CMA-1224

In general, the interstellar extinction in the outer Galaxy is lower than within the solar circle; however, it is higher than average toward the CMA star formation region (Lombardi et al. 2011). For this reason, we investigate the amount of extinction in more detail toward CMA-1224 using the $N(\text{H}_2)$ map from Elia et al. (2013).

Based on the investigation of the extinction law in the Perseus molecular cloud, Foster et al. (2013) found that the extinction law changes from the “diffuse” value of $R_V \sim 3$ to the “dense cloud” $R_V \sim 5$. We adopt the measured $N(\text{H}_2)/E(B - V)$ ratio of $2.9 \times 10^{21} \text{ cm}^{-2}$ (Bohlin et al. 1978) and assume $R_V = A_V/E(B - V)$ of 4.0. We calculate A_V ($N(\text{H}_2)/(7.25 \times 10^{20}) \text{ mag}$) for each pixel in the image; each *Spitzer* source covered by the $N(\text{H}_2)$ image is assigned A_V of the pixel it is associated with. For the remaining sources in the small region at the eastern boundary of CMA-1224, we use the maximum value of A_V in the “off-region” (see below). To calculate A_K from A_V , we use a relation $A_K/A_V = 0.114$ (Weingartner & Draine 2001; $R_V = 4.0$). We use the Flaherty et al. (2007) and Koenig & Leisawitz (2014) empirical extinction laws to determine extinction corrections for *Spitzer* and *WISE* bands, respectively. The resulting A_V ranges from ~ 1.6 to ~ 105 mag; $\sim 87\%$ sources are associated with $A_V < 5$ mag and 0.2% with $A_V > 40$ mag.

These calculations are useful; however, they only provide upper limits for A_V . This is due to the fact that the *Herschel* emission used to construct the $N(\text{H}_2)$ map can include envelope emission from the protostars, which is not part of the interstellar A_V . Also, we do not know whether the sources are on the near or far side of the star-forming region; some of the *Herschel* emission may originate from behind the cloud.

We estimated the maximum A_V of 4.1 mag in the “off-region” indicated with a circle in Figure 3 to represent the interstellar extinction up to the near side of the star-forming cloud. This value is consistent with the high end of the A_K extinction range estimated by Lombardi et al. (2011) toward the CMA star formation region based on the 2MASS data.

5.2. Color-Color Cuts: 2MASS and Spitzer Photometry

We select the IR-excess sources based on a set of three CCDs that combine two 2MASS near-IR and the GLIMPSE360 4.5 μm data: $H - K_s$ versus $K_s - [4.5]$, $J - K_s$ versus $J - [4.5]$, and $J - H$ versus $H - [4.5]$ (Figures 9–11). A combination of these CCDs will allow us to include all *Spitzer* sources with IR excess that have at least two detections in the 2MASS bands.

Some of the sources in the $H - K_s$ versus $K_s - [4.5]$ CCD have diagonal distribution in a direction roughly orthogonal to the reddening vector. We found that this feature corresponds to faint sources with large uncertainties. Unusually large photometric errors (especially at K_s band) randomly shift the true color of the sources along the anti-diagonal in the plot. These sources could be either faint background galaxies or faint halo stars, but they also could be low-luminosity YSOs. For our subsequent analysis, we use 2MASS photometry with uncertainties smaller than 0.2 mag to remove the least reliable photometry.

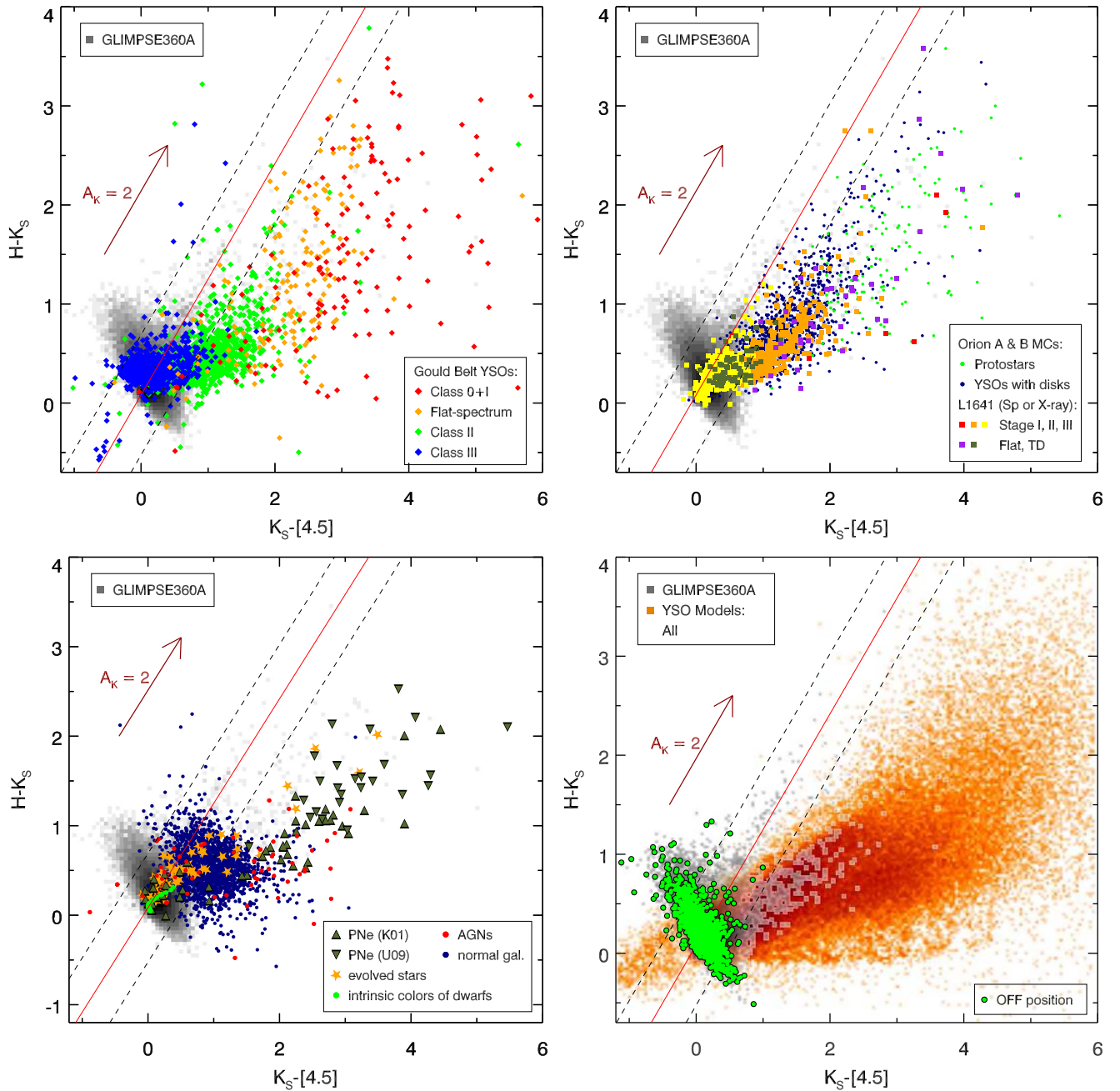


Figure 9. Distribution of the GLIMPSE360 catalog sources (shown in gray as a Hess diagram) in the $H - K_s$ vs. $K_s - [4.5]$ CCD with respect to known Galactic YSOs (Fang et al. 2013; L1641) and YSO candidates (Megeath et al. 2012; Orion A and B molecular clouds; Dunham et al. 2015; 18 nearby molecular clouds from the Gould Belt; top panel), evolved stars and extragalactic sources (Kochanek et al. 2012; Reiter et al. 2015; bottom left), and YSO 2D radiative transfer models (Robitaille et al. 2006; bottom right). In the bottom left panel, we also plot the locus of the intrinsic colors of dwarf stars from Pecaut & Mamajek (2013); we use the $K_s - w2$ color as a proxy of the $K_s - [4.5]$ color. The catalogs from the literature are described in Appendix A. The green circles in the bottom right panel indicate sources detected in the area selected as a representation of the background (“off-region”; see Figure 3). The red solid line is parallel to the reddening vector and originates at the position of the K0 dwarf. Dashed lines represent 1σ uncertainty in color.

The red solid line parallel to the reddening vector in the 2MASS+*Spitzer* CCDs shown in Figures 9–11 originates at the position of the K0 dwarf (Pecaut & Mamajek 2013). The dashed line on either side of the red line in Figures 9–11 represents a 1σ uncertainty in color; we adopt the maximum uncertainty in the colors displayed in each CCD. The sources located between the two dashed lines are expected to be reddened stellar photospheres (see, e.g., Winston et al. 2007; Willis et al. 2013). For further analysis, we select sources rightward from the dashed line on the right in at least one of the

three 2MASS+*Spitzer* CCDs:

$$\left\{ \begin{array}{l} H - K_s < 1.1674 \cdot (K_s - [4.5]) - 0.5240 \text{ or} \\ J - K_s < 0.7774 \cdot (J - [4.5]) - 0.4196 \text{ or} \\ J - H < 1.0758 \cdot (H - [4.5]) - 0.2997 \end{array} \right. \quad (1)$$

Out of $\sim 68,000$ sources, 3144 fulfill the above criteria. We investigate how this number changes when we apply the selection criteria to the dereddened photometry. We deredden the photometry in two ways: (1) for each source, we apply the extinction corrections derived for the associated $N(\text{H}_2)$ pixel;

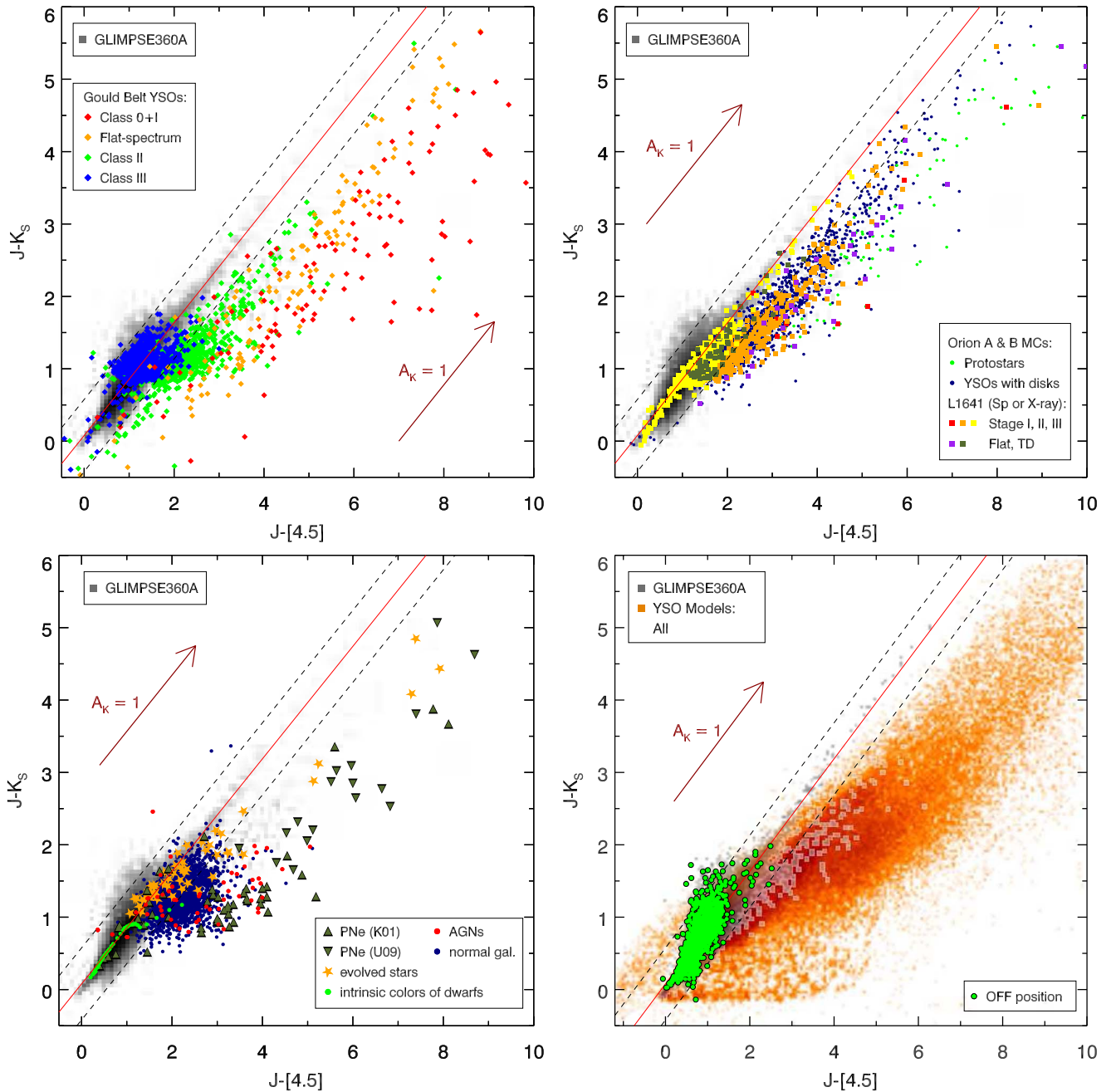


Figure 10. Same set of plots as in Figure 9, but for the $J - K_s$ vs. $J - [4.5]$ CCD.

(2) we calculate the extinction corrections using the maximum value of $N(\text{H}_2)$ in the “off-region” and apply them to all the sources. As discussed in Section 5.1, the extinction corrections estimated based on $N(\text{H}_2)$ are upper limits. For the $H - K_s$ versus $K_s - [4.5]$ color-color cut, only six sources are removed when the dereddened photometry is used (both methods). The results remain the same for the $J - K_s$ versus $J - [4.5]$ color-color cut. For the $J - H$ versus $H - [4.5]$ cut, three more sources are selected for the photometry dereddened using the first method, and two using the second method with two sources overlapping. All but two of the sources removed/added to the list have $[3.6] > 14$ mag and will be removed from the list in the further analysis. Since the difference between the results obtained using the observed and

dereddened (with the extinction corrections being upper limits) photometry is negligible, we use the former in our analysis.

This result is not unexpected since Equation (1) is based on limits that follow the reddening path and the two dereddening methods should provide the same results. The difference of a few sources is likely due to computational round-off errors.

5.2.1. Removing Contaminating Sources

As Figures 9–11 show, the initial list of 3144 YSO candidates is still contaminated by background galaxies; there may also be some contamination from reddened stellar photospheres. We argue, however, that the contamination from evolved stars is negligible.

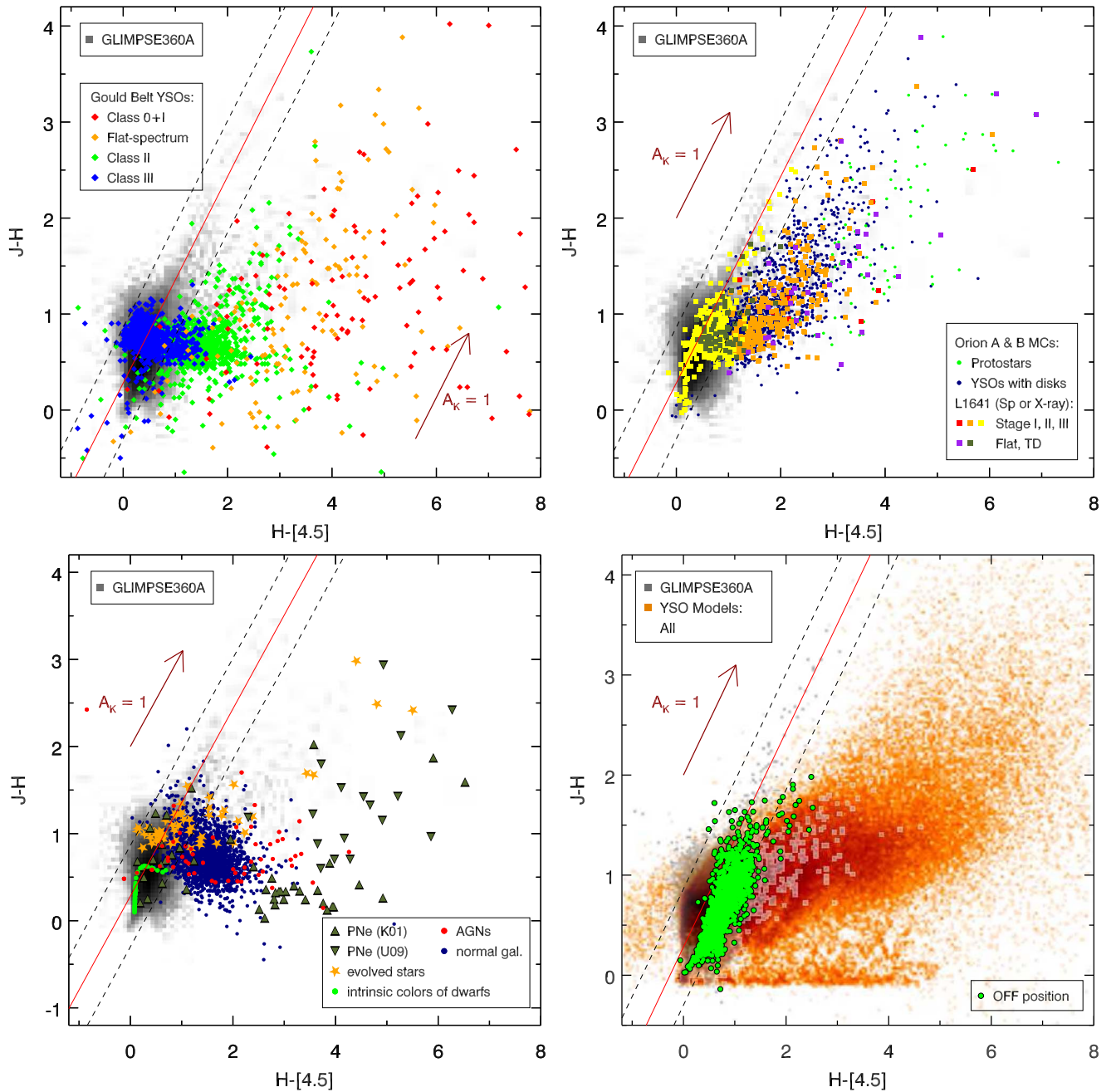


Figure 11. Same set of plots as in Figure 9, but for the $J - H$ vs. $H - [4.5]$ CCD.

Thermally pulsing asymptotic giant branch (TP-AGB) stars can overlap significantly with YSOs in the diagrams using near-IR and mid-IR colors. To estimate the potential contamination from AGB stars in our sample, we use the TRILEGAL stellar population synthesis code (Girardi et al. 2005) updated with the latest COLIBRI TP-AGB models, including circumstellar dust (Marigo et al. 2013). TRILEGAL predicts 69 TP-AGB stars in the direction of our target field (3.5 deg^2). Of these, nine fall within all our 2MASS+*Spitzer* selection criteria (Equations (1) and (2)), and they are also likely to fall within the *WISE* selection criteria based on *WISE* colors of similar TP-AGB stars in the Magellanic Clouds. However, all nine stars are also predicted to be brighter than the survey’s saturation

limit (7 mag at $3.6 \mu\text{m}$), so TP-AGB stars are a negligible source of contamination among our YSO sample.

It is not possible to reliably separate low-luminosity YSO candidates from background galaxies with the photometric data alone. Therefore, we use the $[3.6]$ versus $[3.6]-[4.5]$ CMD to identify regions in the color–magnitude space where the YSOs and background galaxies overlap and remove the latter from our list. This cut makes our YSO candidate list more reliable (less contaminated) but incomplete, as it removes low-luminosity YSOs together with the most likely background galaxies. We also exclude sources overlapping with normal and evolved stars. From the list of the color–color–selected YSO candidates, we keep 234 sources that fulfill the following

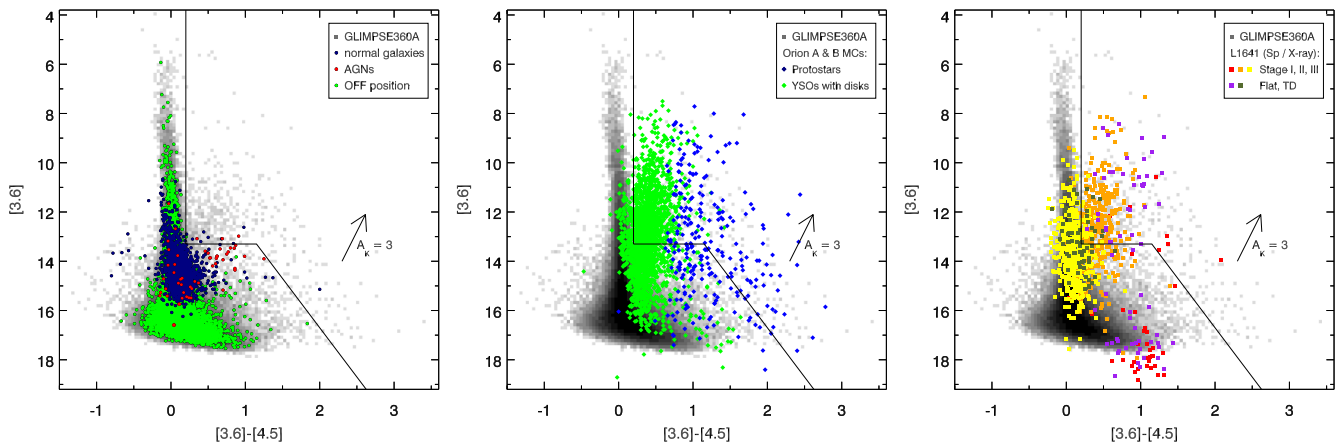


Figure 12. Distribution of the GLIMPSE360 IRAC Archive sources in the [3.6] vs. [3.6]–[4.5] CMD compared to the distribution of normal galaxies, AGNs, and sources from the “off-position” (left; Kochanek et al. 2012), and confirmed and candidate YSOs (middle and right panels; Kochanek et al. 2012; Fang et al. 2013) as indicated in the legends. To minimize a contamination from extragalactic sources and normal stars, we remove objects located to the left of the black lines from our color-selected source list as discussed in Section 5.2.1.

criteria (see Figure 12):

$$\left\{ \begin{array}{l} [3.6] - [4.5] \geq 0.2 \text{ and} \\ [3.6] \leq 13.3 \text{ or } [3.6] \leq 4.0 \cdot ([3.6] - [4.5]) + 8.7 \end{array} \right\}. \quad (2)$$

To remove residual contamination from normally reddened stellar photospheres, we fit the sources’ SEDs with the Castelli & Kurucz (2004) stellar photosphere models using the Robitaille et al. (2007) fitting tool and remove well-fit sources. For the fitting, we use the Weingartner & Draine (2001) extinction law¹⁸ for $R_V = 4.0$ and assume A_V ranging from 0 to 5 mag. We only consider sources with at least four valid data points (not including upper limits; 3143/3144). We quantify how well a source is fit by a given stellar photosphere model SED by considering the value of normalized χ^2 for the best-fitting model per data point ($\chi^2_{\text{best}}/\text{pt}$). We determined the threshold $\chi^2_{\text{best}}/\text{pt}$ of 2 for sources to be well fit and thus removed 11 sources with $\chi^2_{\text{best}}/\text{pt} \leq 2$ from the sample, leaving 223 sources.

5.3. Color–Color Cuts: Spitzer and AllWISE Photometry

We apply additional YSO selection criteria for sources with AllWISE 12 μm data that will allow us to identify younger YSOs without 2MASS detection or sources with low-quality 2MASS photometry. The AllWISE data have been used for the YSO selection in the literature using the [3.4]–[4.6] versus [12]–[22] (or $w1 - w2$ versus $w3 - w4$) CCD, combined with additional criteria aimed at eliminating the background galaxy contamination (e.g., Koenig & Leisawitz 2014; Fischer et al. 2016).

We develop a similar set of the YSO selection criteria based on the GLIMPSE360 3.6 and 4.5 μm and AllWISE 12 μm photometry:

$$\left\{ \begin{array}{l} [3.6] - [4.5] \geq 0.46 \cdot ([4.5] - [12]) - 0.78 \text{ or} \\ [3.6] - [4.5] \geq 0.8 \text{ or} \\ [4.5] - [12] \leq 2.3 \end{array} \right\}. \quad (3)$$

These CCD cuts are shown graphically in Figure 13. As for the objects selected based on the *Spitzer* and 2MASS data, we fit SEDs of 6454 sources that fulfill these criteria and have at

least four data points with the stellar photosphere models and remove well-fit sources. We also apply the criteria listed in Equation (2) to remove background galaxies and normal stars. The *Spitzer*–AllWISE criteria identified 233 YSO candidates; 93 of those are new.

5.4. Detailed Source Inspection

We perform a detailed inspection of the images to assess the environment of the sources selected as YSO candidates and the quality of the photometry (identify artifacts, unresolved/blended sources in the lower-resolution, longer-wavelength bands, etc.). We did not find any technical issues or clear evidence that the sources are not YSOs. The list of YSO candidates for further analysis contains 316 sources.

6. SED Fitting

We fit the SEDs of the YSO candidates with a new set of radiative transfer model SEDs for YSOs developed by Robitaille (2017) using the Robitaille et al. (2007) SED fitting tool. As the Robitaille et al. (2006) set of models that has been widely used to characterize thousands of YSOs and YSO candidates in both the Galaxy and the Magellanic Clouds, the new models span a wide range of evolutionary stages from the youngest, most embedded YSOs to the pre-main-sequence (PMS) stars with little or no disk. The new models, however, include significant improvements. They do not depend on highly model-dependent parameters (such as the stellar age and mass) that depend on stellar evolutionary tracks, but they are defined using parameters that have a direct impact on the radiative transfer. The new models cover a much wider and more uniform region of parameter space and do not introduce correlations between the model parameters. The envelope outer radius for envelope models is now large enough to include 10–20 K dust that is essential for modeling far-IR and submillimeter observations.

Some limitations of the old set of models still remain. The new models still assume a single source of emission (the central star) and do not take into account the effects of the interstellar radiation fields, emission from transiently heated very small grains, and polycyclic aromatic hydrocarbons. The models also assume a single dust model throughout the density structures and do not include accretion explicitly (i.e., only passive disks

¹⁸ <http://www.astro.princeton.edu/~draine/dust/dustmix.html>

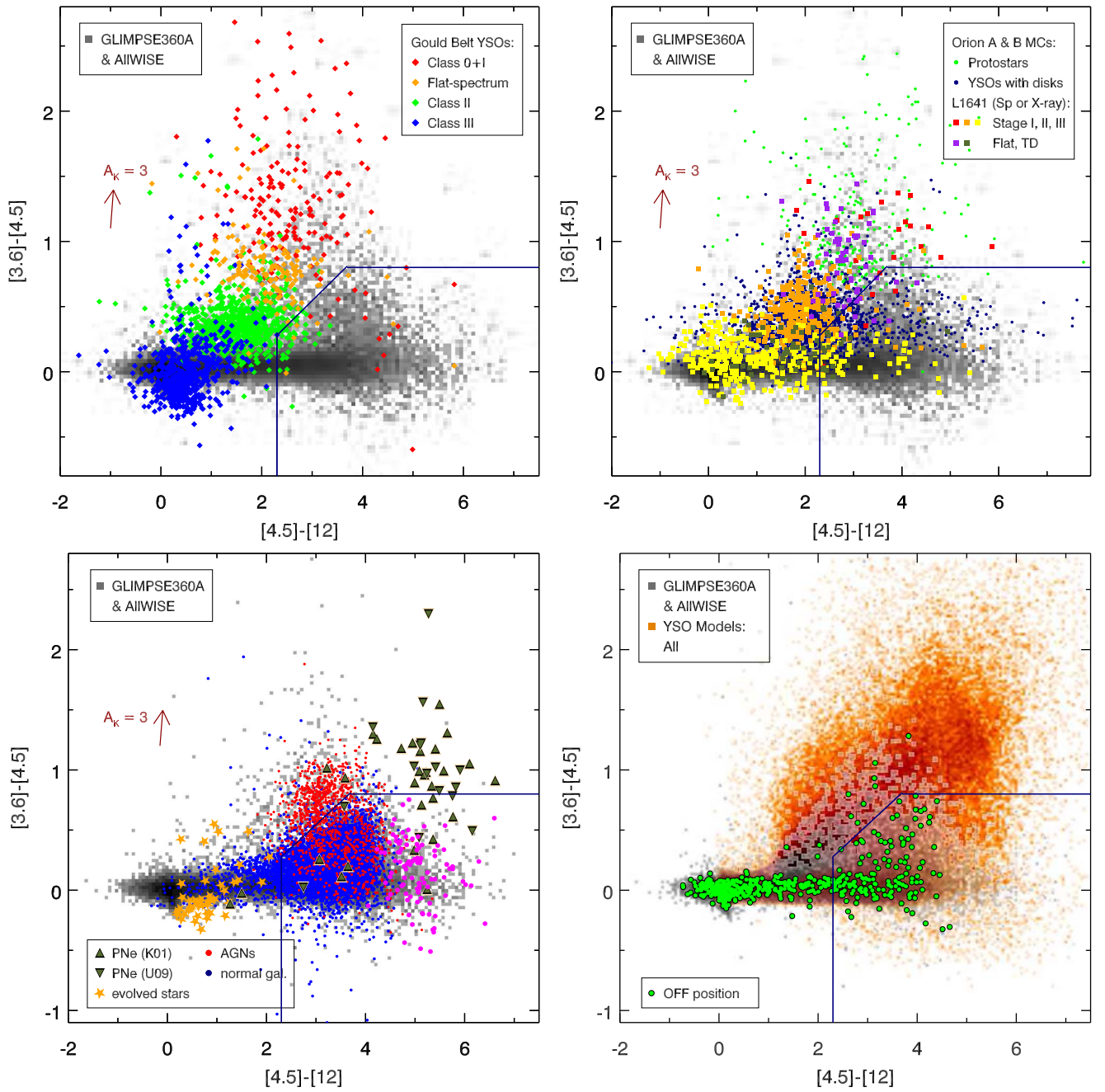


Figure 13. $[3.6]-[4.5]$ vs. $[4.5]-[12]$ CCD showing the YSO (top panel) and non-YSO (bottom left panel) sources from the literature (as indicated in the legends), and the sources from the “off-position” with the *Spitzer*–AllWISE selection criteria overlaid (bottom right panel; Section 5.3). See the Figure 9 caption for references.

are included, and thus the UV and optical fluxes for nonembedded objects cannot be reproduced by the models; Robitaille 2017).

The Robitaille (2017) models consist of a combination of several components: a star, disk, infalling envelope, bipolar cavities, and an ambient medium. They were computed as several sets of models with increasing complexity. The simple model has two parameters, while the most complex model consisting of all of the components has 12.

For the fitting, we allow the distance to vary within 10% from a median value of 0.92 kpc (see Section 4). We consider models with interstellar extinction A_V ranging from 0 to 40 mag in addition to the extinction caused by the YSO’s circumstellar environment that is intrinsic to the models. We use the

Weingartner & Draine (2001) extinction law for $R_V = 4.0$. We only select sources with a $12 \mu\text{m}$ detection, so the fitting can be better constrained. We require at least five valid flux measurements for sources to be included in the analysis. There are 232 sources ($\sim 73\%$ of the color-selected sample) that fulfill both criteria.

The new set of models aims at covering the parameter space as uniformly as possible, but the trade-off is that some of the models are not physical. We select for our fitting procedure only the physical models by comparing their positions on the Hertzsprung-Russell (H-R) diagram with the PARSEC evolutionary tracks (Bressan et al. 2012; Chen et al. 2014, 2015; Tang et al. 2014). The PARSEC evolutionary tracks are produced by the revised Padova code and include the PMS

Table 3
Results of the SED Fitting

Model Set ^a	No. of Sources	Components	Group
s— —s—i	21	star	...
sp— —s—i	72	star + passive disk; $R_{\text{inner}} = R_{\text{sub}}$ ^b	<i>d</i>
sp— —h—i	28	star + passive disk; variable R_{inner}	<i>d</i>
s— —smi	1	star + medium; $R_{\text{inner}} = R_{\text{sub}}$...
sp— —smi	47	star + passive disk + medium; $R_{\text{inner}} = R_{\text{sub}}$	<i>d</i>
sp— —hmi	26	star + passive disk + medium; variable R_{inner}	<i>d</i>
s—p—smi	1	star + power-law envelope + medium; $R_{\text{inner}} = R_{\text{sub}}$	<i>e</i>
s—p—hmi	0	star + power-law envelope + medium; variable R_{inner}	<i>e</i>
s—pbsmi	2	star + power-law envelope + cavity + medium; $R_{\text{inner}} = R_{\text{sub}}$	<i>e</i>
s—pbhmi	5	star + power-law envelope + cavity + medium; variable R_{inner}	<i>e</i>
s—u—smi	2	star + Ulrich envelope + medium; $R_{\text{inner}} = R_{\text{sub}}$	<i>e</i>
s—u—hmi	2	star + Ulrich envelope + medium; variable R_{inner}	<i>e</i>
s—ubsmi	0	star + Ulrich envelope + cavity + medium; $R_{\text{inner}} = R_{\text{sub}}$	<i>e</i>
s—ubhmi	4	star + Ulrich envelope + cavity + medium; variable R_{inner}	<i>e</i>
spu—smi	11	star + passive disk + Ulrich envelope + medium; $R_{\text{inner}} = R_{\text{sub}}$	<i>d+e</i>
spu—hmi	4	star + passive disk + Ulrich envelope + medium; variable R_{inner}	<i>d+e</i>
spubsmi	3	star + passive disk + Ulrich envelope + cavity + medium; $R_{\text{inner}} = R_{\text{sub}}$	<i>d+e</i>
spubhmi	3	star + passive disk + Ulrich envelope + cavity + medium; variable R_{inner}	<i>d+e</i>

Notes.

^a The model set names from Robitaille (2017). Seven characters in the model set names indicate which component is present; they are (in order): s—star; p—passive disk; p or u—power-law or Ulrich envelope; b—bipolar cavities; h—inner hole; m—ambient medium; and i—interstellar dust. A dash (—) is used when a component is absent.

^b R_{inner} is the inner radius for the disk, envelope, and the ambient medium—when one or more of these components are present. R_{sub} is the dust sublimation radius.

stage; the initial stellar masses range from 0.1 to $350 M_{\odot}$ (Bressan et al. 2012; Chen et al. 2015). The YSO models located outside the coverage of the PARSEC PMS tracks are excluded.

The SED fitting results are highly degenerate. To find the best-fitting model, we use a Bayesian approach to assign relative probabilities to the various models of increasing complexity; the technical details and the philosophy behind them are described in Robitaille (2017). In short, for each source after fitting every model from all the model sets, we first find the smallest χ^2 , namely, χ^2_{best} . We define “good” fits as those with $\chi^2 < (\chi^2_{\text{best}} + F)$, where F is a threshold parameter that is determined empirically. In our case, it is found that $F = 3$ is a reasonable choice. We count the number of good fits provided by each model set, and the one with the largest number of good fits is selected as the best model set. The single best model is the one with the smallest χ^2 from the best model set. Note that this single best model may not be the one with χ^2_{best} . That means, instead of directly using χ^2_{best} to determine the best model, we first find the best model set, and from that set we select the best model. The reason is that each model set represents a combination of components (e.g., with envelope, disk), and the most probable model set should be able to give the largest number of reasonably good fits, even if the single χ^2_{best} is not found from there. On the contrary, the single χ^2_{best} could be just a coincidence from a model set where most of the other fits are actually bad. In addition, we note that we at most have 10 photometric data points for each source for the vast majority of the sample, but some of the model sets have up to 13 parameters. Overfitting might occur especially for the sources with fewer data points.

Table 3 lists the Robitaille (2017) model sets and their components, along with the number of sources well fit with models from a given model set. For the subsequent analysis, we divide sources into three groups depending on the presence of

the envelope and/or disk: “envelope-only” (*e* in Table 3; 16 sources), “envelope and disk” (*d + e*; 21 sources), and “disk-only” (*d*; 173 sources). Sources in the “*e*” group might have a disk, but one was not needed to fit their SEDs. Twenty-two sources are well fit with models that contain only a star (21) or a star and an ambient medium (1). We remove these sources from the YSO candidate list; 294 sources remain (210 YSO candidates well fit with YSO models and 84 YSO candidates for which the SED fitting was not performed owing to the lack of photometry at $12 \mu\text{m}$ or too few data points). Example SEDs for YSO candidates at different evolutionary stages are shown in Figure 14.

6.1. Luminosity, Mass, and Age Estimation

The new set of models does not provide the stellar luminosity, mass, and age. First, we find the luminosity for each model with the Stephan–Boltzmann law using the stellar radius and effective temperature that are given. Then, on the H-R diagram the closest PMS track to each model is found. The mass is taken as that of the closest track. The age is interpolated from the closest point on the track to the model on the H-R diagram.

We compare the ages estimated from the evolutionary tracks to the results of the SED fitting, i.e., the presence of an envelope and/or disk, and adopt masses only for sources for which the ages are consistent with the evolutionary stage of the YSO candidates. We adopt YSO lifetimes determined by Dunham et al. (2015) based on a sample of ~ 3000 YSO candidates from nearby star-forming regions. They calculated the lifetimes of 0.46–0.72 Myr for Class 0 + I sources and 0.30–0.46 Myr for flat-spectrum sources, adopting the Class II + III as a reference class with the duration of 3 Myr. The durations of the Class 0 and Class I phases are 0.335 and $0.665 \times$ the Class 0 + I lifetime, respectively. For simplicity, we assume that all the “envelope-only” sources are Class 0

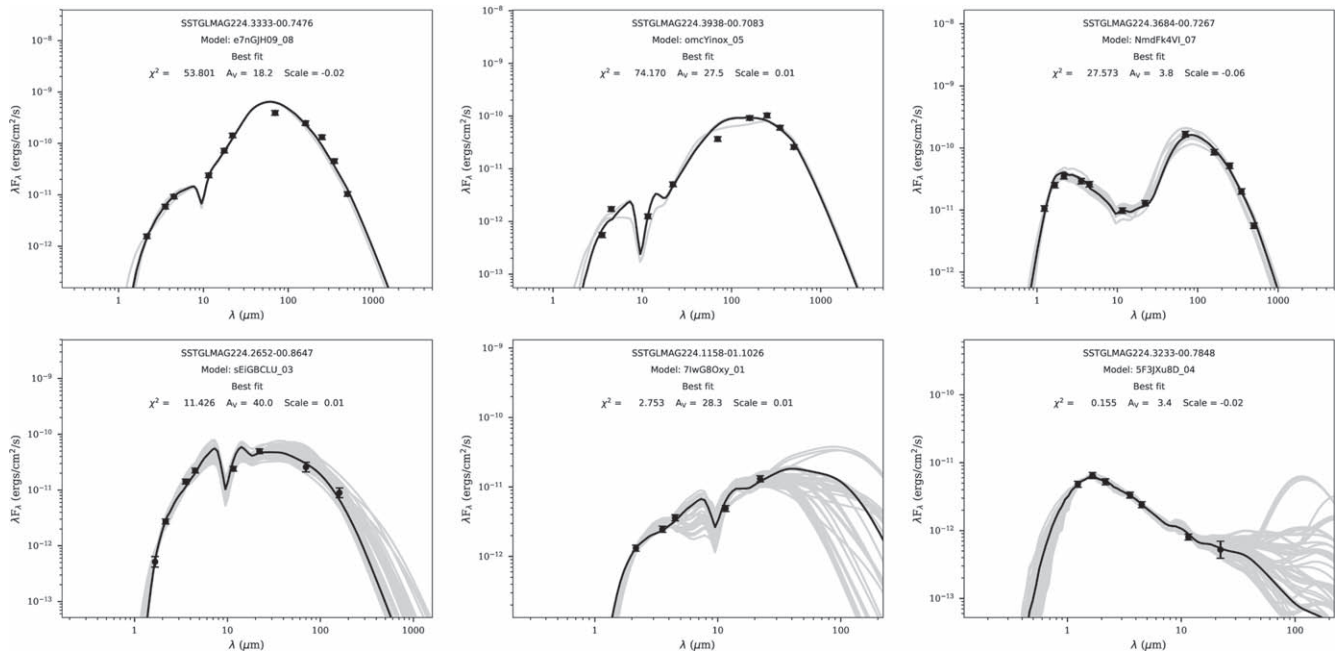


Figure 14. Example SEDs for sources at different evolutionary stages well fit with Robitaille (2017) YSO models. The embedded objects with envelopes but no disks (Group *e*) are shown in the top left and top middle panels. The best-fit model for the source in the top right panel contains both an envelope and a disk (Group *d + e*). The bottom row shows SEDs of sources best fit with models with disks, but not envelopes (Group *d*). The solid black line in each panel shows the best-fit YSO model. Filled circles and triangles are valid flux values and flux upper limits, respectively. The values of a reduced χ^2 , interstellar visual extinction, and a distance scale for the best-fit model are indicated in the plots. The flux error bars are plotted if larger than the data points. See Section 6 for details.

YSOs, “envelope and disk” sources are Class I or flat-spectrum YSOs, and “disk-only” sources are Class II and Class III YSOs.

The physical parameters estimated from the SED fitting and the H-R diagram analysis for 210 YSO candidates are listed in Table 4.

7. SIMBAD Search

We searched the SIMBAD database for matches within 5'' from the *Spitzer*/GLIMPSE360 positions of 294 YSO candidates from our list to check whether the sources have been classified in the literature. We have found four matches with known sources that were not from the Elia et al. (2013) or Fischer et al. (2016) catalogs.

Source SSTGLMAG 224.4696–00.3780 is classified in the literature as a Be star (HD 55135; e.g., Frémat et al. 2006); we removed it from the list of YSO candidates.

Source SSTGLMAG 225.3263–00.5314 has been identified in the literature as a galaxy (2MASX J07122445–1115336; e.g., Paturel et al. 2003), a massive YSO with an extended bipolar H₂ emission (MSX6C G225.3266–00.5318; Navarete et al. 2015), and a *Herschel*/Hi-GAL protostellar core (G225.32629–00.53244; Elia et al. 2013). Since the extragalactic nature of this source is not confirmed, we keep the source on the list of YSO candidates.

Source SSTGLMAG 224.3005–00.8417 was identified as a member of the EX Lupi-like class of YSO outbursts by Miller et al. (2015): iPTF 15afq. These outbursts, with a duration from a few weeks to several months, are interpreted as the accretion events driven by disk instabilities (e.g., Audard et al. 2014). The EX Lupi objects have circumstellar disks and no envelopes; this is consistent with the results of the SED fitting.

Source SSTGLMAG 225.1412–01.3289 coincides with a radio source, PMN J0709–1128 (Wright et al. 1996; Vollmer et al. 2010 and references therein), with a spectral index α

between 1.4 and 4.9 GHz of 0.32 ($S_\nu \propto \nu^{-\alpha}$; Vollmer et al. 2010). The extragalactic nature of this source is not ruled out (Petrov et al. 2011), but we keep it on the list of YSO candidates with a warning that the classification is uncertain.

In summary, based on the SIMBAD search, we removed one source from the list of YSO candidates; 293 sources remain on the list. Their spatial distribution is shown in Figure 15. All the photometry used in the analysis is provided in Table 5.

8. Classification of YSO Candidates in Color–Color Space

In Table 5, we provide the Class I and Class II classification for YSO candidates from our list based on the classification criteria from the literature. For sources with valid 12 μ m photometry, we use the Fischer et al. (2016) criteria; otherwise, the classification is based on the Gutermuth et al. (2009) criteria. We include a flag indicating which criteria were used. Four sources do not fulfill either Fischer et al. (2016) or Gutermuth et al. (2009) criteria; they are classified as YSO candidates with disks based on the SED fitting.

We use the Gutermuth et al. (2009) criteria for Class I and Class II based on the ($K_s - [3.6]_0$) versus ($[3.6] - [4.5]_0$) CCD (see Figure 16), where the subscript “0” indicates dereddened colors. The extinction is estimated based on the 2MASS colors (they require at least *H* and *K_s* photometry and magnitude uncertainties < 0.1 mag). To minimize the contamination from extragalactic sources, they apply the brightness limit using dereddened 3.6 μ m photometry: $[3.6]_0 < 15.0$ and $[3.6]_0 < 14.5$ for Class I and Class II YSO candidates, respectively.

The Fischer et al. (2016) criteria, a slightly modified version of the Koenig & Leisawitz (2014) criteria, use the *WISE* $w1 - w2$ versus $w2 - w3$ CCD (see Figure 17). We replace the *WISE* bands $w1$ and $w2$ with GLIMPSE360 3.6 μ m and 4.5 μ m bands, respectively.

Table 4
Physical Parameters for a Subset of YSO Candidates in CMa–I224

IRAC Designation “SSTGLMC”	n_{pt}^{a}	Model Set ^b	Model Name	$(\chi_{\text{min}}^2/\text{pt})_{\text{set}}^{\text{c}}$	$(n_{\text{fits}})_{\text{set}}^{\text{d}}$	R_{\star} (R_{\odot})	T_{\star} (T_{\odot})	L_{\star} (L_{\odot})	M_{\star}^{e} (M_{\odot})	Age ^e (Myr)
G223.4100–00.9594	5	spu–smi	O9yTeubb_01	0.363	132	1.63	3690	0.443
G223.4356–00.9369	6	sp–s–i	bRpK1icY_01	0.0262	461	0.939	4180	0.243
G223.4467–00.9365	6	spu–hmi	lceeyFSO_03	3.69	30	7.99	6880	129	4	0.766
G223.4519–00.9364	18	spubhmi	UYPUxRp7_07	2.93	13	12.3	6270	210	5.2	0.275
G223.4894–00.8837	7	sp–hmi	szXsXcnT_09	0.743	68	1.4	5740	1.92
G223.5416–00.7255	7	sp–h–i	ddJqkFr2_03	1.41	42	2.03	5520	3.43	1.7	3.93
G223.5622–00.9594	7	sp–s–i	r9oRQITx_03	0.135	328	2.61	9610	52.2	2.4	3.85
G223.5881–00.9575	6	sp–smi	5FMrwNtB_08	0.0817	664	1.78	5900	3.46
G223.7198–00.8560	7	sp–s–i	J29C1Wcg_04	0.581	353	1.24	6300	2.16
G223.7210+00.0052	7	sp–hmi	74RteWgE_07	0.841	32	0.975	5020	0.544

Notes.

^a n_{pt} is the number of valid data points used for the fitting.

^b See Table 3 footnotes for the meaning of characters in the model set names.

^c $(\chi_{\text{min}}^2/\text{pt})_{\text{set}}$ is χ^2 per data point for the best-fit model from the most likely model set.

^d $(n_{\text{fits}})_{\text{set}}$ is the number of fits with χ^2/pt between $(\chi_{\text{min}}^2/\text{pt})_{\text{set}}$ and $(\chi_{\text{min}}^2/\text{pt})_{\text{set}} + 2$ in the most likely model set.

^e We provide stellar masses (M_{\star}) and ages (Age) only for sources with the most reliable estimates of these parameters (see Section 6.1 for details).

(This table is available in its entirety in machine-readable form.)

The YSO candidates from our list are overplotted on the CCDs used for the classification: $(K_s - [3.6])_0$ versus $([3.6] - [4.5])_0$ in Figure 16 (Gutermuth et al. 2009) and $[3.6] - [4.5]$ versus $[4.5] - [12]$ in Figure 17 (Fischer et al. 2016).

The top panels show CCDs with YSO candidates identified in Dunham et al. (2015; left), Fang et al. (2013; middle), and Megeath et al. (2012; right).

9. [3.6][4.5]-only Sources

About 56% of the GLIMPSE360 Archive sources with both 3.6 and 4.5 μm photometry do not have matches in any of the other catalogs; thus, we cannot apply to them the YSO selection criteria described above. These sources may be too faint in the near-IR to be detected by 2MASS, which is not a good match for the high-sensitivity GLIMPSE360 survey. However, a nondetection at shorter wavelengths may also indicate the sources’ youth, making them interesting targets for future studies. Although we cannot provide strong evidence that any of these sources are YSOs, we make an effort to identify the best candidates.

In this analysis, we also include *Spitzer* sources that have AllWISE matches but no valid 12 and 22 μm photometry (not in the catalog or of poor quality and removed) and no matches in other catalogs.

We only consider GLIMPSE360 Archive sources that are also present in the highly reliable GLIMPSE360 Catalog (see Section 2.1) to make sure that all the [3.6][4.5]-only sources are legitimate astronomical objects with the highest-quality photometry. We found Catalog counterparts for 125,918 out of 133,152 (or $\sim 95\%$) Archive sources; 74% of these Catalog sources still have both 3.6 and 4.5 μm photometry. The Catalog has higher S/N thresholds and slightly more stringent acceptance criteria. Less reliable fluxes present in the Archive were removed from the Catalog. The subsequent analysis includes 92,962 sources and uses the Catalog photometry.

The left panel of Figure 18 shows the distribution of all GLIMPSE360 Catalog sources in CMa–I224 and a subset with the 3.6 and 4.5 μm photometry only in the [3.6] versus [3.6]–[4.5] CMD. For comparison, the middle panel shows the

distribution of Catalog sources from the “off-position” in the same CMD. The “off-position” represents the background/foreground populations. We apply color–magnitude cuts listed in Equation (2) to remove background galaxies (see the right panel of Figure 18). We consider the remaining 47 sources as “possible YSO candidates”

The spatial distribution of the [3.6][4.5]-only possible YSO candidates is shown overlaid on the H_2 column density image in Figure 19. The vast majority of the sources are associated with the highest $N(\text{H}_2)$ regions, coincident with clusters of YSO candidates; this location supports their classification as possible YSO candidates.

Table 6 provides the *Spitzer*/GLIMPSE360 IRAC Catalog photometry for [3.6][4.5]-only sources that we identified as “possible YSO candidates.” For sources in regions covered by the H_2 column density map, the value of the $N(\text{H}_2)$ pixel a given *Spitzer* source is associated with is also listed; it may be useful to identify the most interesting/reliable sources for follow-up studies.

We searched the SIMBAD Astronomical Database to check whether any of the [3.6][4.5]-only possible YSO candidates are associated with a known astronomical object. We used a search radius of 5” and found only three matches. Two of the sources are associated with IRAS sources (IRAS 07067–1040 and IRAS 07077–1026) and one with the Elia et al. (2013) *Herschel* core (G224.48274–00.63637), all at distances $>4''$ (see Table 6). Therefore, we do not remove any sources based on the SIMBAD search.

10. A Comparison to the WISE YSO Candidate List

Ninety-three WISE YSO candidates from Fischer et al. (2016) are located within CMa–I224. We match these sources to our final list of YSO candidates using the AllWISE designation. Twenty out of 93 WISE sources are not present (not matched to the GLIMPSE360 sources) in our list of YSO candidates. A detailed comparison between the two catalogs, including AllWISE designations, is provided in Appendix C.

Twelve of the AllWISE sources identified as YSO candidates by Fischer et al. (2016) were matched to the

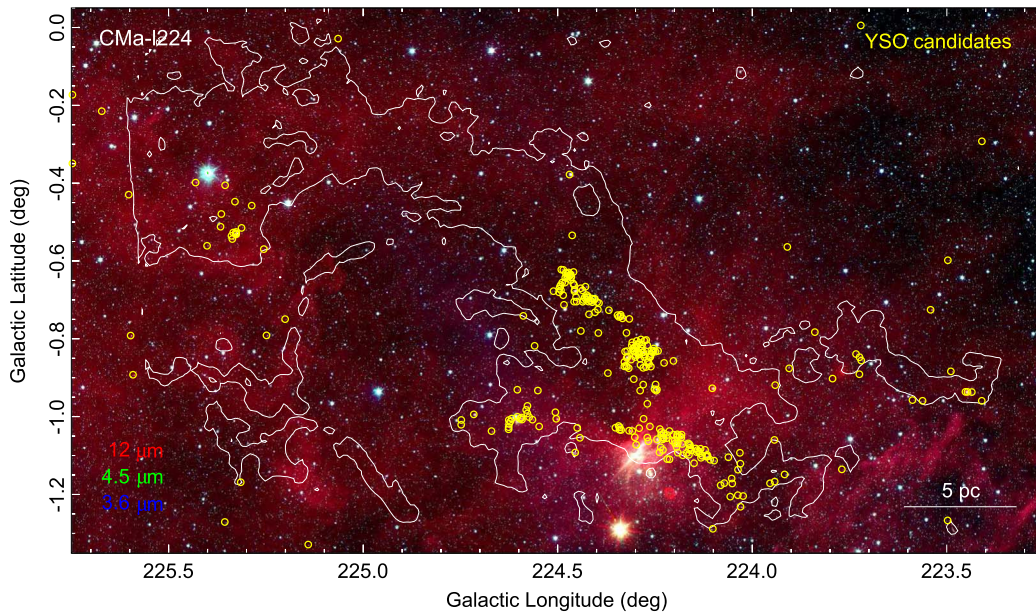


Figure 15. Three-color composite image of CMA-*l*224 combining the *WISE* 12 μm (red), GLIMPSE360 4.5 μm (green), and GLIMPSE360 3.6 μm (blue) images; the same as in Figure 3. The positions of YSO candidates identified in this paper are indicated with yellow circles. The white contour corresponds to the H_2 column density of $4 \times 10^{21} \text{ cm}^{-2}$.

GLIMPSE360 sources with distances larger than $1''$; the matches were not considered real, and AllWISE photometry was not used. Two of these GLIMPSE360 sources were identified as YSO candidates based on *Spitzer* and 2MASS photometry and are on our final list, and four sources are on the [3.6][4.5]-only list of “possible YSO candidates.” One [3.6][4.5]-only source does not have a GLIMPSE360 Catalog counterpart and was removed from the list of “possible YSO candidates” (see Section 9 for the selection criteria). The remaining five sources (without the AllWISE photometry) do not fulfill one of our YSO selection criteria (see Appendix C for details).

Five AllWISE sources were matched to GLIMPSE360 sources within $1''$, and both the *Spitzer* and AllWISE photometry was used in the analysis. Two of these sources were removed as background galaxy candidates. Three sources are on our final list of YSO candidates, but the AllWISE matches/photometry were removed during the analysis.

Two out of 20 *WISE* sources do not have a *Spitzer* detection, and one was resolved into two *Spitzer* sources.

In summary, five of the GLIMPSE360 sources that were initially matched to the “missing” Fischer et al. (2016) sources are on our list of YSO candidates, and four are on the [3.6][4.5]-only list of “possible YSO candidates” (indicated in Table 6). One [3.6][4.5]-only source was removed owing to the lack of a GLIMPSE360 Catalog counterpart. Seven GLIMPSE360 sources that were initially matched to AllWISE sources were removed from the list based on the 2MASS and GLIMPSE360 photometry. Three Fischer et al. (2016) sources do not have a clear *Spitzer* counterpart.

11. YSO Candidates versus *Herschel* Filaments

A wealth of filamentary structures are detected in CMA-*l*224 as in other regions in the Galaxy (Molinari et al. 2010). Filaments can be identified in the *Herschel* images using algorithms designed to extract features with a filamentary shape (e.g., Schisano et al. 2014; Koch & Rosolowsky 2015). It is

worth noting that a term “filament” is widely adopted in the literature, but it still lacks a precise definition.

Schisano et al. (2014) identified filaments in the region of the Galactic plane studied by Elia et al. (2013) that covers CMA-*l*224. They define a “filament” as an extended 2D feature in the H_2 column density map with an elongated, cylinder-like shape and a relatively high contrast with respect to the background emission. They define filament “branches” as the group of segments tracing the skeleton of the filamentary region and as a “spine,” a subset of branches forming the main axis of the region. They adopted the algorithm based on the Hessian matrix to identify the filament extraction algorithm as regions of the map where the shape of the emission has a downward concavity, resembling the appearance of a cylinder. Schisano et al. (2014) measured the physical properties of the filaments, finding that these structures cover a wide range of lengths (~ 1 to ~ 30 pc), widths (0.1 to 2.5 pc), and average column densities ($\sim 10^{20}$ to $\sim 10^{22} \text{ cm}^{-2}$). This work has recently been revised by Schisano et al. (2018), who developed the catalog of the filamentary structure candidates extracted from the *Herschel* Hi-GAL images over the entire Galactic plane (Schisano et al. 2018).

A total of 212 filament candidates from Schisano et al. (2018) are located in the region $223^\circ 3 \leq l \leq 225^\circ 8$ corresponding to CMA-*l*224; they are shown in the top panel of Figure 20, overlaid on the H_2 column density map they were identified on. The contours represent the filament candidate borders that are extended with respect to the position traced by the algorithm in order to find the position where the filamentary emission merges with the background. The width of the contours in Figure 20 is a function of contrast (“*C*”), i.e., the ratio between the intensity along the filament branches and its border (Schisano et al. 2018). The thick contours indicate features with $C > 1.1$ (or contrast $> 10\%$ of the average background level), which are the most robust, while the thin contours indicate features with $C \leq 1.1$. In CMA-*l*224, we found 78, 94, and 40 features with $C \leq 1.1$, $1.1 \leq C \leq 1.25$, and $C \geq 1.25$, respectively.

Table 5Data from the 2MASS, *Spitzer*/GLIMPSE360, ALLWISE, AKARI, MSX, and *Herschel*/Hi-GAL Point Source Catalogs and the Classification of YSO Candidates

Column	Name	Description
1	IRACDesignation	GLIMPSE360 IRAC Archive source name: “SSTGLMA GLLL.llll ± BB.bbbb,” where LLL.llll and BB.bbbb are the galactic longitude and latitude, respectively
2	R.A.(J2000)	R.A., J2000 (degrees)
3	Decl.(J2000)	Decl., J2000 (degrees)
4	Objid_2MASS	Identification number for a 2MASS source (cntr in the IRSA/GATOR)
5	Objid_ALLWISE	“designation” from the ALLWISE catalog
6	Objid_AKARI	“objname” from the AKARI catalog
7	Objid_MSX	“MSX6C_ID” from the MSX catalog
8	Objid_HerschelE13	<i>Herschel</i> source identification number from Elia et al. (2013)
9	Dist_GL360-ALLWISE	Distance between GLIMPSE360 and ALLWISE matching sources (arcsec); a null value is -9.999
10	Dist_GL360-AKARI	Distance between GLIMPSE360 and AKARI matching sources (arcsec); a null value is -9.999
11	Dist_GL360-MSX	Distance between GLIMPSE360 and MSX matching sources (arcsec); a null value is -9.999
12	Dist_GL360-HerschelE13	Distance between GLIMPSE360 and Elia et al. (2013) <i>Herschel</i> matching sources (arcsec); a null value is -9.999
13	Dist_GL360-HerschelFull	Distance between GLIMPSE360 and <i>Herschel</i> Full matching sources (arcsec); a null value is -9.999
14–27	mag $_i$, dmag $_i$	2MASS JHK_s ($i = 1-3$), GLIMPSE360 IRAC 3.6 and 4.5 μm ($i = 4-5$), ALLWISE 12 and 22 μm ($i = 6-7$); a null value for mag $_i$ and dmag $_i$ is 99.999. For magnitudes corresponding to flux upper limits, the magnitude uncertainties are set to -999.9 .
28–63	flux $_i$, dflux $_i$	2MASS JHK_s ($i = 1-3$), GLIMPSE360 IRAC 3.6 and 4.5 μm ($i = 4-5$), ALLWISE 12 and 22 μm ($i = 6-7$), AKARI 9 and 18 μm ($i = 8-9$), MSX ($i = 10-13$), Hi-GAL PACS 70 and 160 μm ($i = 14-15$), and SPIRE 250, 350, and 500 μm ($i = 16-18$) fluxes and flux uncertainties (mJy); a null value for flux $_i$ and dflux $_i$ is -999.9 . For flux upper limits, flux $_i > 0$ and dflux $_i = -999.9$.
64	Classification_SED_Fitting	YSO classification based on the SED fitting: envelope-only (“e”), disk and envelope (“d + e”), and disk-only (“d”)
65	Classification_Phot	Class I (“I”) and Class II (“II”) classification of YSO candidates based on the criteria from the literature. When the 12 μm data are available, the Fischer et al. (2016) criteria are used; otherwise, the sources are classified based on the Gutermuth et al. (2009) criteria.
66	Classification_Phot_Ref	Flag indicating what criteria were used to determine the YSO class provided in the “Classification_Phot” column: F16—Fischer et al. (2016); G09—Gutermuth et al. (2009)

(This table is available in its entirety in machine-readable form.)

The large number of structures in CMA-1224 indicates that the dense clouds in the region have a significant number of filamentary substructures, many of which might not be identified owing to the coarse spatial resolution of the *Herschel* H₂ column density map (36”). The limited spatial resolution of this data set also makes the association between the filaments and *Spitzer* YSOs uncertain, as the positions of the latter are generally known with $\sim 1''$ accuracy. To overcome these issues, we applied the filament identification algorithm to the *Herschel*/SPIRE 250 μm image, which is one of the images that clearly shows a filamentary network and has a two times higher spatial resolution than the H₂ column density image (18”). We adopt a similar set of parameters to that in Schisano et al. (2018), where the extraction was done over the column density map of the entire Galactic plane.

After visual inspection of the initial results, we decide to redo the analysis with a slightly lower threshold value. The threshold level is given in terms of the local standard deviation of the eigenvalue of the Hessian matrix. We lowered the threshold from 3 times the standard deviation used by Schisano et al. (2018) to 2.7. The lower threshold level adopted in this work slightly changes the number of identified structures, but more importantly it merges adjacent regions that appeared to be connected to a visual inspection. The goal of the filament extraction based on the 250 μm image is to improve the reliability of associating the *Spitzer* sources with *Herschel* filaments rather than determining the physical parameters of the latter; thus, we do not extend the filament borders to encompass the entire filament emission, but we only trace the innermost regions of the filamentary structures where the emission has a

downward concavity. This approach allows us to better estimate the position of the branches forming the skeleton of the region.

The bottom panel of Figure 20 shows the *Herschel* 250 μm image with contours outlying the filamentary structures identified using the method described above. There is a good correspondence between the features extracted based on the H₂ column density map (top panel of Figure 20) and those based on the 250 μm image, but the latter shows more substructures as a result of the better spatial resolution. Figure 21 shows a zoom-in on the densest clouds in the center of CMA-1224 with the positions of the *Spitzer* YSOs and *Herschel* filaments extracted from the 250 μm image (left panel) and the filament branches (right panel) indicated. The vast majority of the YSO candidates are located in the proximity of the filament branches, indicating that stars likely form along the filaments as suggested by André et al. (2014). The dense cores, the precursors of the stars, are mostly found along or at the intersection of filaments (e.g., Könyves et al. 2015).

To investigate whether our results are consistent with this star formation scenario, we measure the YSO distances from the filament branches. Figure 22 shows the distance histograms color-coded by the YSO evolutionary stage as defined in Section 6: “envelope-only” (the youngest YSOs dominated by the emission from the circumstellar envelope), “envelope and disk” (more evolved YSOs with the contribution from both the envelope and the disk), and “disk-only” (the most evolved YSOs in our sample). Our results indicate that younger YSOs, those with envelopes and envelopes+disks, are found within $\sim 30''$ from filament branches. This angular distance

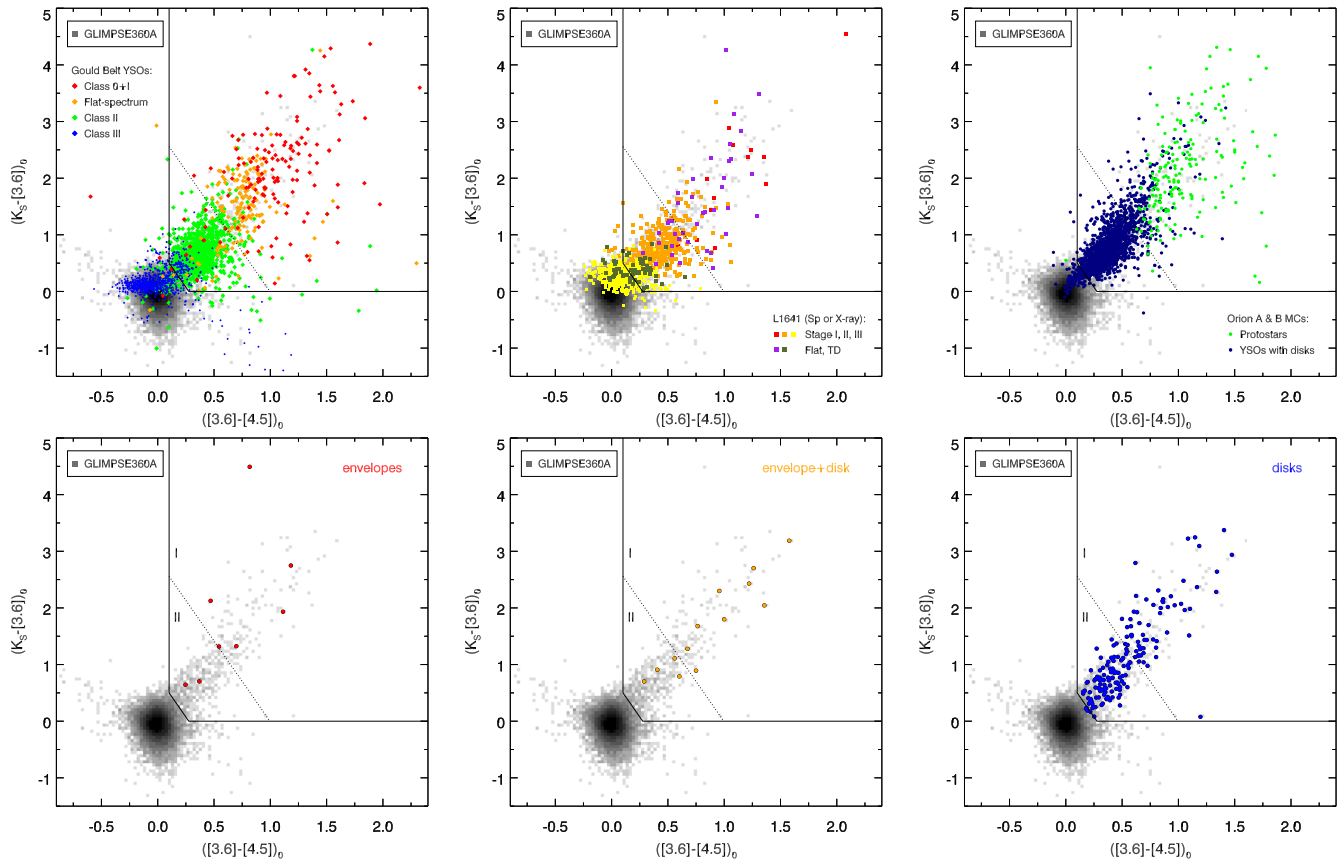


Figure 16. Distribution of the GLIMPSE360 IRAC Archive sources in the $K_s - [3.6]$ vs. $[3.6]-[4.5]$ CCD; the photometry has been corrected for extinction using “method 2” (see Section 5). Black solid lines show the YSO classification criteria developed by Gutermuth et al. (2009) to classify sources with no longer-wavelength IRAC photometry available. The black dotted line separates Class I and Class II YSO candidates. The top panels show CCDs with YSO candidates identified in Dunham et al. (2015; left), Fang et al. (2013; middle), and Megeath et al. (2012; right). The YSO candidates identified in CMA-I224 (see Sections 5–6) are plotted in the CCDs in the bottom panels: “e” (left), “d+e” (middle), and “d” (right). See text for details.

corresponds to 0.15 pc at a distance of 1 kpc, close to the characteristic width of ~ 0.1 pc of filaments in nearby clouds (e.g., André 2017 and references therein). The older population of disk-only YSOs is more spread out with a wide range of distances from the filament branches. The spatial distribution of YSO candidates as a function of the evolutionary stage is shown in Figure 23.

The fact that the younger population of YSOs is closely associated with the central regions of the filaments while the oldest YSOs are more widely distributed supports the idea that stars are formed in the filaments and become more dispersed with time. Similar results are found in nearby star-forming regions like Taurus (Hartmann 2002), Orion (Salji et al. 2015), Lupus (Benedettini et al. 2015), and Corona Australis (Bresnahan et al. 2018).

12. Maser, Molecular Line, and Continuum Observations from the Literature

To put the results of our work into broader context, we collect information from the literature on the maser, molecular line, and continuum observations overlapping with the CMA-I224 region.

12.1. Water Masers and SiO Emission

Two 22 GHz H_2O masers from the Arcetri Catalog are within the boundaries of CMA-I224 (Valdettaro et al. 2001; 32 m Medicina telescope, HPBW $\sim 1'9$). They were observed toward

two *IRAS* sources: IRAS 06040–1241 and IRAS 06011–1445. IRAS 06040–1241 is associated with the main filament, while IRAS 06011–1445 is located close to the southern boundary of the region. The latter source is classified in SIMBAD as a star (BD –14 1318, TYC 5361-812-1); it is saturated in *Spitzer* and *WISE* images and coincides with a *Herschel* source.

Harju et al. (1998) detected SiO ($J = 2-1$) and ($J = 3-2$) emission toward the position of the H_2O maser in the main filament with the SEST telescope (HPBW $\sim 57''$ and $40''$, respectively). The detection of the SiO emission indicates the presence of shocks.

12.2. CS Emission

The CS (2–1) emission was detected toward five *IRAS* sources with the SEST telescope (HPBW $\sim 50''$) in the Bronfman et al. (1996) survey of the *IRAS* point sources with the characteristics of UC H II regions. All of the *IRAS* sources detected in CS are associated with *Herschel* filaments (see Figure 24). The correlation between the CS emission and the most active star formation sites is expected since CS is a tracer of the high molecular gas column density.

12.3. Planck Cold Cores

Sixteen cold cores from the *Planck* Catalog of Galactic Cold Clumps are located in CMA-I224 (Planck Collaboration et al. 2016; 350, 550, and $850 \mu\text{m}$, HPBW $\sim 4'8$, $4'7$,

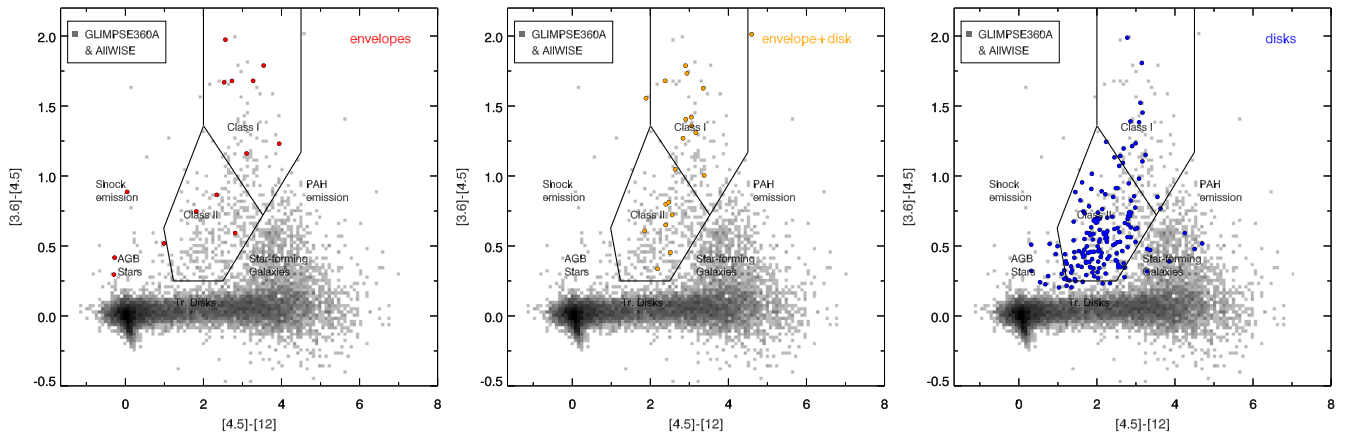


Figure 17. $[3.6]-[4.5]$ vs. $[4.5]-[12]$ CCDs showing the distribution of all GLIMPSE360 sources with AllWISE matches with the AllWISE YSO selection criteria from Fischer et al. (2016) overlaid. We use the GLIMPSE360 3.6 and 4.5 μm bands rather than AllWISE $w1$ and $w2$ bands. The YSO candidates classified as “e” (left), “d+e” (middle), and “d” (right) based on the SED fitting are overlaid (see Section 6). The AGB stars can be found between $[3.6]-[4.5] = 0$ and 2, and they can also be red in $[4.5]-[12]$, but we only expect a small contamination from AGB stars.

and 4/3, respectively). As expected, *Planck* cores (extracted from the images convolved to a common $5'$ resolution), tracing cold dust within dense regions in the molecular clouds, are well correlated with the *Herschel* emission. Two of the clumps overlap with regions with a high concentration of outflows traced by the 4.5 μm emission in the main *Herschel* filament: PGCC G224.28–0.82 and PGCC G224.48–0.63 (see Figure 24). Zahorecz et al. (2016) identified PGCC G224.48–0.63 as a potential site of massive star and cluster formation based on the empirical mass–size threshold of massive star formation proposed by Kauffmann & Pillai (2010).

12.4. CO Emission

Olmi et al. (2016) selected the two most prominent *Herschel*/Hi-GAL filaments from Elia et al. (2013) for follow-up CO observations. These filaments are located in CMa–I224, and they were mapped in ^{12}CO , ^{13}CO , C^{18}O , and C^{18}O ($J = 1-0$) lines with the MOPRA radio telescope at a $38''$ resolution. Olmi et al. (2016) studied the main filament associated with the largest number of the Hi-GAL protostellar clumps and the nearby, more quiescent (“secondary”) filament associated with starless clumps (see Figures 6 and 25). Our results confirm the evolutionary status of these filaments; the main filament is associated with a large number of YSO candidates, including the youngest sources in the region, while no YSO candidates are identified in the secondary filament.

Olmi et al. (2016) found that the *Herschel* protostellar clumps are more luminous and more turbulent than the starless clumps, and they lie in regions where the ambient gas has broader lines.

Olmi et al. (2016) observations cover two out of three regions associated with the extended 4.5 μm emission (likely outflows from YSO candidates) and *Herschel* protostellar clumps/cores; all three regions are indicated in Figure 25, where the CO emission is compared to the 12 and 4.5 μm emission (see also Figure 4). Olmi et al. (2016) detected the velocity gradients along the filaments; however, they did not find any strong evidence for accretion flows feeding these two main YSO candidate/*Herschel* cores/clumps clusters located in the main filament.

Based on the analysis of the gravitational stability of the filaments, Olmi et al. (2016) concluded that the main, higher-density filament (thermally supercritical and gravitationally bound) is at a later stage of evolution than the secondary filament (unbound or near to virial equilibrium and hosts less turbulent ambient gas), consistent with the evolutionary stages of the associated Hi-GAL clumps.

13. Star Formation in CMa–I224

The presence of the $\text{H}\alpha$ expanding shell and the absence of luminous stars at the center of expansion led Herbst & Assousa (1977) to propose that star formation in the CMa OB1/R1 complex was triggered by a supernova event. The main filament in CMa–I224 lies at the rim of the $\text{H}\alpha$ shell, hinting at a possible connection between the supernova event and star formation in the region.

The stars in the CMa R1 association lie between the kinematic center of the expansion and the densest concentration of molecular gas, where star formation is ongoing. Herbst & Assousa (1977) identified a runaway star, HD 54662 (Figure 1), that could be associated with the event that produced the supernova remnant. They estimated an age of the supernova shell of 5×10^5 yr by comparing the observed physical properties of the shell in the CMa OB1/R1 complex to the models of supernova remnants evolving in a uniform medium.

The scenario of the supernova-induced star formation was supported by a study by Herbst et al. (1978), who derived similar ages for most of the members of the R1 association; the positions of stars with respect to the shell were also consistent with the model proposed by Herbst & Assousa (1977). However, the later study by Shevchenko et al. (1999) showed that the distribution of CMa R1 candidate members in the H-R diagram indicates a large spread in stellar ages, which is inconsistent with a scenario of a single burst of star formation induced by a shock wave. They found that only a small fraction of young stars in the CMa R1 association could have been created by the supernova explosion, which indicates that the supernova-induced star formation is a minor process in this region. Shevchenko et al. (1999) further argue that even in the presence of external compression, quiescent cloud collapse seems to be more efficient.

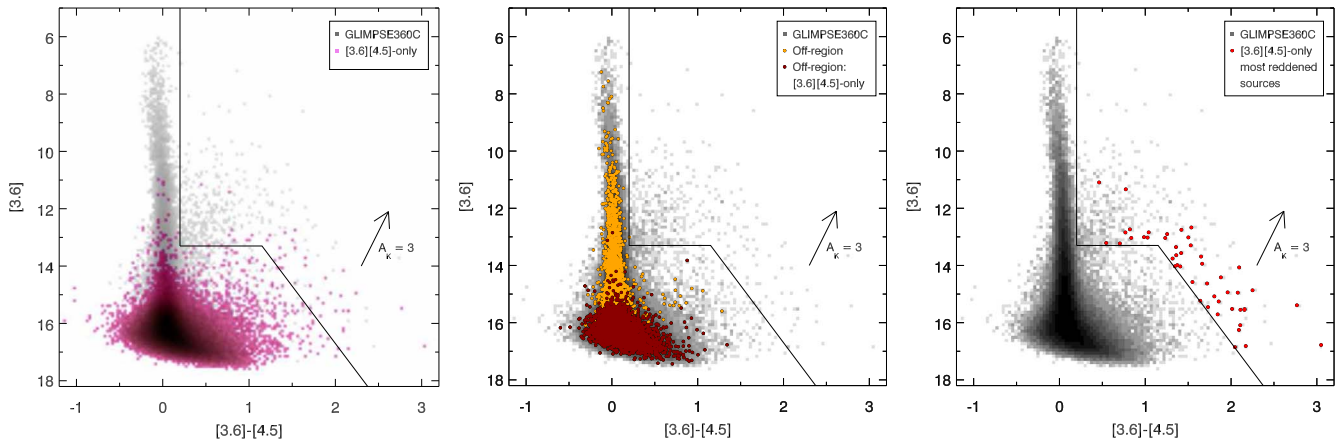


Figure 18. [3.6] vs. [3.6]-[4.5] CMDs showing the distribution of the GLIMPSE360 Catalog (rather than the less reliable but more complete Archive) sources in CMa- τ 224 (gray in all panels). The [3.6][4.5]-only Catalog sources are shown in pink as a Hess diagram in the left panel. The middle panel shows all the GLIMPSE360 Catalog sources in the “off-position” (see Figure 3) that represent the background sources in yellow and those with [3.6][4.5]-only photometry in red. We select sources located to the right of the black solid line indicated in all panels (Equation (2); see also Section 5.2.1) as potential YSO candidates (plotted in red in the right panel); more firm classification requires further investigation. See Section 9 for details.

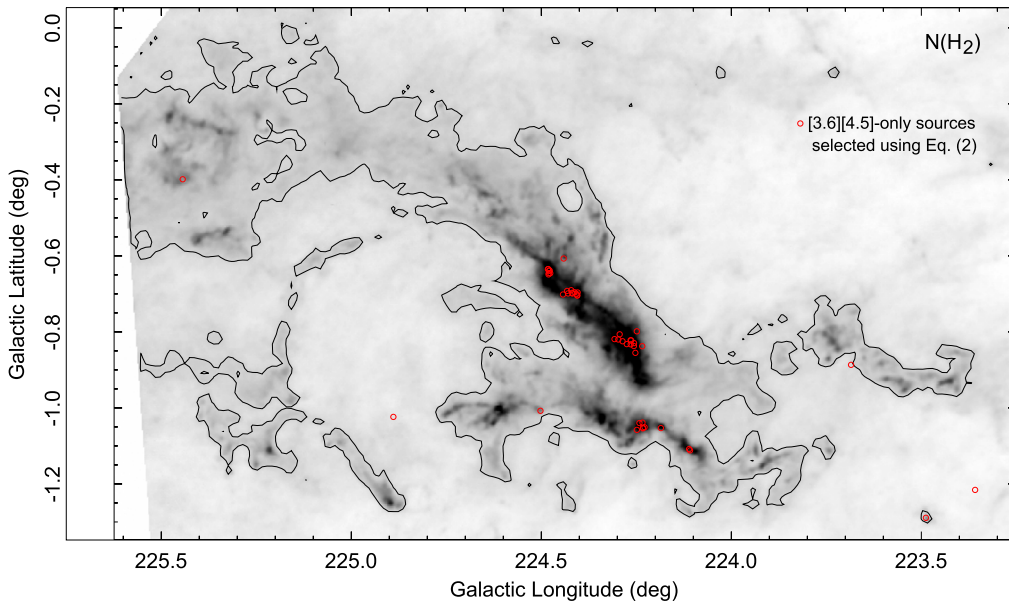


Figure 19. Distribution of [3.6][4.5]-only sources selected as “possible” YSO candidates using Equation (2) (red circles; see also Figure 18) overlaid on the H_2 column density image. The black contour corresponds to $N(H_2)$ of $4.0 \times 10^{21} \text{ cm}^{-2}$.

An alternative scenario of the origin of the shell in CMa R1 was proposed by Reynolds & Ogden (1978), who studied the kinematics, temperature, and ionization state of gas based on the $H\alpha$, [N II], and [O III] lines. They estimated a radius of the shell of ~ 34 pc (assuming a distance of 1.1 kpc), a temperature of ~ 8000 K, and an expansion velocity of $\sim 13 \text{ km s}^{-1}$, ionized by two O stars in the CMa OB1 association. They argue that although their observations are consistent with the hypothesis that the shell was produced by a supernova explosion that triggered star formation in the region, models involving strong stellar winds or an evolving H II region are not ruled out. Another possible explanation of the nature of the shell was proposed by Nakano et al. (1984). Based on the radio continuum observations, they showed that OB stars in the area are sufficient to ionize the whole nebula. Similarly to the Reynolds & Ogden (1978) study, Nakano et al. (1984) results are still consistent with the supernova scenario.

Some further evidence supporting the supernova-induced star formation was provided by Comeron et al. (1998), who studied the patterns of expanding motions in the CMa OB1/R1 complex measured by the *Hipparcos* satellite. They found that the spatial arrangement and age of different structures in the CMa OB1 association, the kinematic pattern, the existence of runaway stars, and the energetic requirements implied by the observed motions are all compatible with the supernova explosion. Comeron et al. (1998) found an expansion center of the shell at $(l, b) \sim (226^\circ.5, -1^\circ.6)$, an expansion velocity of $\sim 15 \text{ km s}^{-1}$, and an approximate age of 1.5 Myr. They found the existence of a new runaway star revealed by its large proper motion directed away from the center of expansion, further supporting the supernova scenario.

Fischer et al. (2016) studied the $10^\circ \times 10^\circ$ region centered on the Canis Major star-forming region with *WISE* 3.4–22 μm data. They identified 144 Class I and 335 Class II YSO

Table 6
The *Spitzer* GLIMPSE360 IRAC Catalog Photometry of “Possible YSO Candidates” in CMA-1224

IRAC Designation “SSTGLMC”	R.A. (deg, J2000)	Decl. (deg, J2000)	$F_{3.6\ \mu\text{m}}$ (mJy)	$\sigma_{F_{3.6\ \mu\text{m}}}$ (mJy)	$F_{4.5\ \mu\text{m}}$ (mJy)	$\sigma_{F_{4.5\ \mu\text{m}}}$ (mJy)	[3.6] (mag)	σ [3.6] (mag)	[4.5] (mag)	σ [4.5] (mag)	$N(\text{H}_2)$ ($10^{21}\ \text{cm}^{-2}$)
G223.3585–01.2156	106.56161	–9.82876	0.169	0.027	0.755	0.054	15.55	0.17	13.44	0.08	2.5
G223.4879–01.2890 ^a	106.55575	–9.97743	2.256	0.282	3.076	0.088	12.74	0.14	11.92	0.03	8.29
G223.6849–00.8865	107.01062	–9.96732	0.221	0.027	0.782	0.08	15.26	0.13	13.4	0.11	3.88
G224.1086–01.1116	107.00566	–10.44693	8.202	0.404	10.69	0.417	11.34	0.05	10.56	0.04	22.69
G224.1110–01.1081	107.00999	–10.44751	1.349	0.058	3.531	0.081	13.3	0.05	11.77	0.03	24.75
G224.1854–01.0529 ^a	107.09463	–10.48809	2.224	0.089	5.264	0.127	12.75	0.04	11.33	0.03	25.07
G224.2321–01.0525	107.11684	–10.52937	1.731	0.104	2.851	0.131	13.03	0.07	12	0.05	31.25
G224.2282–01.0508	107.11656	–10.52519	0.94	0.123	2.748	0.155	13.69	0.14	12.04	0.06	41.42
G224.2329–01.0535	107.11625	–10.53055	0.294	0.017	1.276	0.079	14.95	0.06	12.87	0.07	31.25
G224.2337–01.0385	107.13019	–10.52436	0.688	0.08	1.518	0.102	14.03	0.13	12.68	0.07	27.78
G224.2344–00.8375	107.31198	–10.43238	0.169	0.02	0.785	0.07	15.55	0.13	13.4	0.1	12.06
G224.2417–01.0397	107.13287	–10.53207	0.226	0.028	0.657	0.059	15.23	0.13	13.59	0.1	36.41
G224.2524–00.8550	107.30466	–10.4564	0.103	0.008	0.459	0.013	16.09	0.09	13.98	0.03	74.17
G224.2485–01.0577	107.11986	–10.54636	1.455	0.077	1.538	0.1	13.21	0.06	12.67	0.07	28.44
G224.2485–00.7983	107.35396	–10.42686	1.754	0.074	2.78	0.072	13.01	0.05	12.03	0.03	22.41
G224.2560–00.8293	107.32951	–10.44776	0.414	0.039	1.104	0.059	14.58	0.1	13.03	0.06	71.58
G224.2564–00.8370	107.32273	–10.45165	2.398	0.086	6.317	0.177	12.67	0.04	11.13	0.03	68.13
G224.2636–00.8223	107.33935	–10.45124	0.713	0.033	1.617	0.05	13.99	0.05	12.62	0.03	69.69
G224.2648–00.8325	107.33072	–10.45707	0.055	0.006	0.578	0.03	16.78	0.13	13.73	0.06	83.2
G224.2650–00.8219	107.34042	–10.45236	1.937	0.061	3.94	0.105	12.9	0.03	11.65	0.03	60.77
G224.2751–00.8320	107.33607	–10.46596	0.185	0.018	0.582	0.036	15.46	0.11	13.72	0.07	94.93
G224.2862–00.8244 ^a	107.34805	–10.47232	0.663	0.029	2.916	0.092	14.07	0.05	11.97	0.03	82.63
G224.2938–00.8062	107.36805	–10.47061	2.049	0.079	3.417	0.102	12.84	0.04	11.8	0.03	52.83
G224.2973–00.8198	107.35741	–10.48002	1.714	0.117	2.37	0.09	13.04	0.07	12.2	0.04	60.76
G224.3074–00.8188	107.36304	–10.48851	0.981	0.054	2.198	0.063	13.64	0.06	12.28	0.03	53.08
G224.4056–00.7035	107.51322	–10.52242	0.297	0.036	1.155	0.152	14.94	0.13	12.98	0.14	41.17
G224.4071–00.7001	107.51694	–10.52218	0.088	0.015	0.388	0.057	16.25	0.18	14.16	0.16	54.81
G224.4045–00.6961	107.51929	–10.51803	1.275	0.064	2.847	0.094	13.36	0.05	12	0.04	61.7
G224.4053–00.7043	107.51229	–10.52257	0.481	0.054	1.74	0.14	14.42	0.12	12.54	0.09	36.93
G224.4127–00.6954	107.52379	–10.52505	0.395	0.036	1.232	0.059	14.63	0.1	12.91	0.05	72.02
G224.4182–00.6989	107.52321	–10.53149	0.196	0.027	1.602	0.117	15.39	0.15	12.62	0.08	68.11
G224.4186–00.6969	107.52527	–10.53095	0.317	0.042	1.612	0.108	14.87	0.14	12.62	0.07	80.2
G224.4213–00.6901	107.53262	–10.53017	0.174	0.019	0.71	0.067	15.52	0.12	13.51	0.1	47.39
G224.4295–00.6986	107.52878	–10.54137	2.047	0.07	2.656	0.086	12.84	0.04	12.08	0.04	33.02
G224.4322–00.6921	107.536	–10.54081	0.173	0.024	0.806	0.113	15.53	0.15	13.37	0.15	33.15
G224.4429–00.7014	107.53261	–10.55457	0.146	0.009	0.511	0.03	15.71	0.06	13.87	0.06	27.22
G224.4412–00.6068	107.61717	–10.50934	0.051	0.004	0.214	0.013	16.86	0.08	14.81	0.07	15.23
G224.4764–00.6455	107.59878	–10.55849	0.683	0.065	1.599	0.065	14.04	0.1	12.63	0.04	49.1
G224.4817–00.6345	107.61111	–10.55808	0.882	0.041	1.9	0.078	13.76	0.05	12.44	0.05	59.15
G224.4798–00.6389	107.60636	–10.55844	0.261	0.015	0.88	0.038	15.08	0.06	13.28	0.05	62.66
G224.4780–00.6384	107.60594	–10.55656	1.433	0.047	1.752	0.046	13.23	0.04	12.53	0.03	62.66
G224.4802–00.6451	107.60091	–10.5617	1.051	0.039	2.484	0.069	13.57	0.04	12.15	0.03	52.52
G224.4827–00.6351	107.61112	–10.55922	1.74	0.067	4.438	0.16	13.02	0.04	11.52	0.04	59.15
G224.4810–00.6486	107.5981	–10.56394	0.745	0.077	2.207	0.143	13.94	0.11	12.28	0.07	48.45
G224.5022–01.0075	107.28408	–10.74833	1.711	0.056	3.406	0.154	13.04	0.04	11.81	0.05	9.37
G224.8892–01.0235	107.45126	–11.09911	0.053	0.006	0.249	0.013	16.82	0.13	14.64	0.06	3.18
G225.4435–00.3982 ^a	108.27774	–11.30138	10.22	0.245	10.02	0.219	11.1	0.03	10.63	0.02	8.05

Note.

^a Sources SSTGLMC G224.1854–01.0529, SSTGLMC G224.2862–00.8244, SSTGLMC G225.4435–00.3982, and SSTGLMC G223.4879–01.2890 correspond to *WISE* YSO candidates J070822.75–102916.3, J070923.42–102818.8, J071306.61–111803.8, and J070613.51–095837.9, respectively, from Fischer et al. (2016).

(This table is available in its entirety in machine-readable form.)

candidates in this 100 deg² region, with 53% of the sources organized in 16 groups of more than four members. Four out of 16 groups have more than 25 members. Fischer et al. (2016) found that the distribution of the *WISE* YSO candidates is consistent with supernova-induced star formation; however, the Class II/Class I ratios in different regions are unexpected provided that they trace age. They conclude that this quantity depends on the initial conditions if the supernova explanation is correct.

The *Spitzer* YSO sources associated with extended 4.5 μm emission indicating outflows are members of the group Fischer et al. (2016) identified as “Group 00” with the largest number of members (41). Our analysis shows that Group 00 is not a single group, but rather two (possibly three) different YSO candidate clusters.

We dub regions with the high concentration of YSO candidates in the upper, middle, and lower section of the main filament “cluster A,” “cluster B,” and “cluster C,” respectively

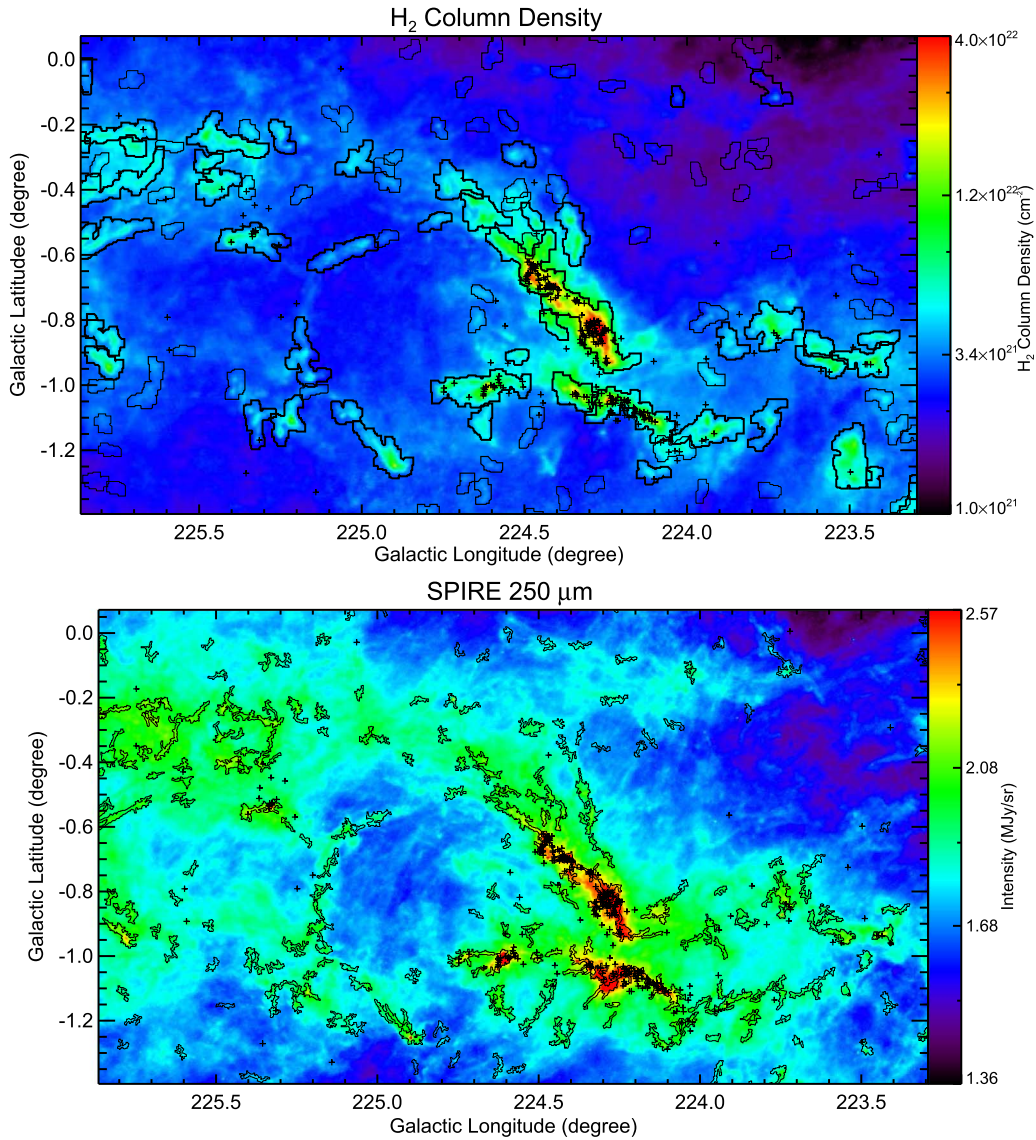


Figure 20. Distribution of YSO candidates with respect to the filaments identified based on the H_2 column density map (top; Schisano et al. 2014) and the *Herschel* 250 μm image (bottom; this paper and Schisano et al. 2018). The boundaries of the filaments are indicated with black contours and the positions of YSOs with black plus signs. The vast majority of the YSO candidates are associated with the three brightest filaments in the region.

(see Figure 25; the sizes of the clusters indicated in the image are arbitrary). All the sources in these three clusters are the Fischer et al. (2016) Group 00 members.

Each cluster is associated with an *IRAS* source (A: IRAS 07081–1028; B: IRAS 07077–1026; C: IRAS 07070–1024), with the *IRAS* source positions offset from the cluster’s center in Cluster A and C (see Figure 24). Cluster B is the most compact, while Cluster C is the most extended. Both Cluster A and Cluster C are associated with a *Planck* source (Section 12.3). Cluster B was not detected with *Planck*, but it is associated with the H_2O maser and the SiO emission (SiO observations were targeted toward the H_2O maser; see Section 12.1)—both considered as good protostellar outflow tracers, confirming the ongoing outflow activity in the region. *IRAS* sources in Clusters A and B were observed in CS (2–1), and the CS emission was detected toward both sources (see Section 12.2).

Olmi et al. (2016) CO observations cover Clusters B and C, but not Cluster A (see Section 12.4 and Figure 25). The ^{12}CO emission peaks coincide with Clusters B and C; the ^{12}CO

emission is brighter toward Cluster C. The C^{18}O emission that traces the dense gas peaks toward this cluster, while significantly fainter C^{18}O emission is detected toward Cluster B (see Figure 25).

The properties of the YSO candidate clusters in the main filament indicate that Cluster B, with the reduced molecular gas reservoir and association with the H_2O maser, may be at a later evolutionary stage than Clusters A and C.

The Olmi et al. (2016) CO observations indicate that Cluster B is located at the intersection of two filaments—the main filament associated with *Herschel* protostellar cores and YSO candidates (including Clusters A, B, and C), and a more quiescent filament associated with pre-stellar cores, directed toward northeast from the main filament and connected with it near Cluster B’s position (see Olmi et al. 2016). Olmi et al. (2016) detected a velocity gradient from northwest to southeast (from Cluster C toward Cluster B) along the main filament and along the secondary filament in the direction of Cluster B in the main filament. These velocity gradients hint at the possibility of the filamentary accretion. The star formation in the main

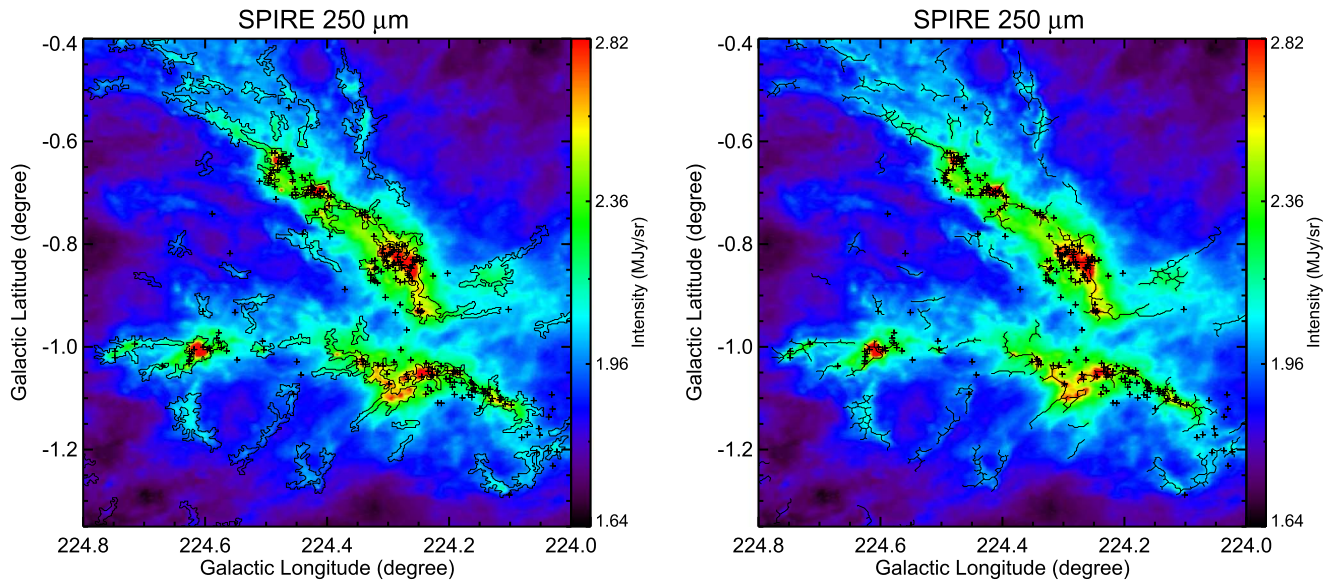


Figure 21. Left: same image as in the bottom panel in Figure 20, zoomed in on the three brightest filaments. Right: 250 μm image with the filament “skeletons” (black solid lines) and YSO candidate positions (plus signs) indicated.

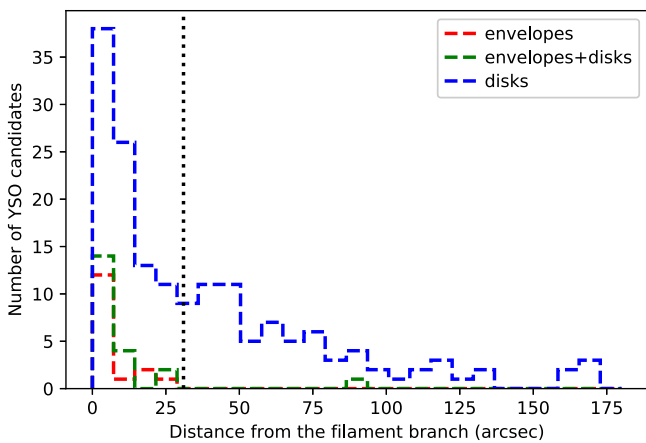


Figure 22. Histograms of distances from the filament branches for YSO candidates well fit with YSO models containing envelopes only (red), envelopes+disks (green), and disks only (blue). The vertical dotted line corresponds to $31''$ or 0.15 pc at a distance of 1 kpc.

filament might have started at the location of Cluster B, where mass would be accreted from both the main and secondary filaments.

The positional coincidence between the main filament in CMa-1224 and the $\text{H}\alpha$ shell indicates that there may be a connection between the supernova event in the CMa OB1/R1 association and star formation in CMa-1224. According to one of the theories of filament formation, the filaments are formed by the large-scale compression of the interstellar material in supersonic magnetohydrodynamic flows, which can be turbulent or nonturbulent (e.g., André 2017 and references therein). The waves from the supernova explosion are possible driving sources for the large-scale turbulence (e.g., Rybakin & Goryachev 2018); thus, the filaments in CMa-1224 could have been formed as a result of the supernova event in the CMa OB1/R1 association. The formation of the filament is followed by the gravitational fragmentation and the formation of pre-stellar cores, the precursors of stars. Such a two-step star formation scenario (i.e., the filament formation followed by the

prestellar core formation by gravitational instability) is supported by the results of the *Herschel* studies on filaments (e.g., André 2017).

One of the kinematic signatures of filament formation within shock-compressed layers generated by large-scale supersonic flows are velocity gradients in the direction perpendicular to the main axis of the filament in addition to those along the filaments (e.g., Chen & Ostriker 2014; Inutsuka et al. 2015). Such kinematic patterns were detected in the molecular line observations of the filaments (e.g., Kirk et al. 2013; Palmeirim et al. 2013). The transverse velocity gradients are often observed along the entire length of the filaments. The Olmi et al. (2016) single-dish observations show some indication of the transverse velocity gradients in the C^{18}O data; however, higher-resolution observations are needed to draw reliable conclusions.

In an alternative scenario, star formation in CMa-1224 could have been induced by the supernova in the preexisting filaments or, if no supernova event happened in Canis Major as some studies suggest, by the spontaneous gravitational collapse of the filaments. The latter scenario is supported by the ages of the YSO candidates, e.g., in the main filament, half of the YSO candidates have ages longer than the highest estimate of the supernova remnant’s age (i.e., 1.5 Myr; Comeron et al. 1998).

14. Summary

Using *Spitzer*/GLIMPSE360 3.6 and 4.5 μm data, combined with 2MASS JHK_s , AllWISE 12 and 22 μm , and *Herschel*/Hi-GAL 70–500 μm data, we identify YSO candidates in a 3.5 deg^2 region in the Canis Major OB1 association, which we dubbed CMa-1224. CMa-1224 contains the largest concentration of sources associated with extended 4.5 μm emission (an outflow tracer) in the entire GLIMPSE360 survey that coincides with bright *Herschel* filaments.

Our YSO selection method is based on *Spitzer*–2MASS and *Spitzer*–AllWISE color–color cuts, combined with the visual inspection of the images and a set of criteria to remove

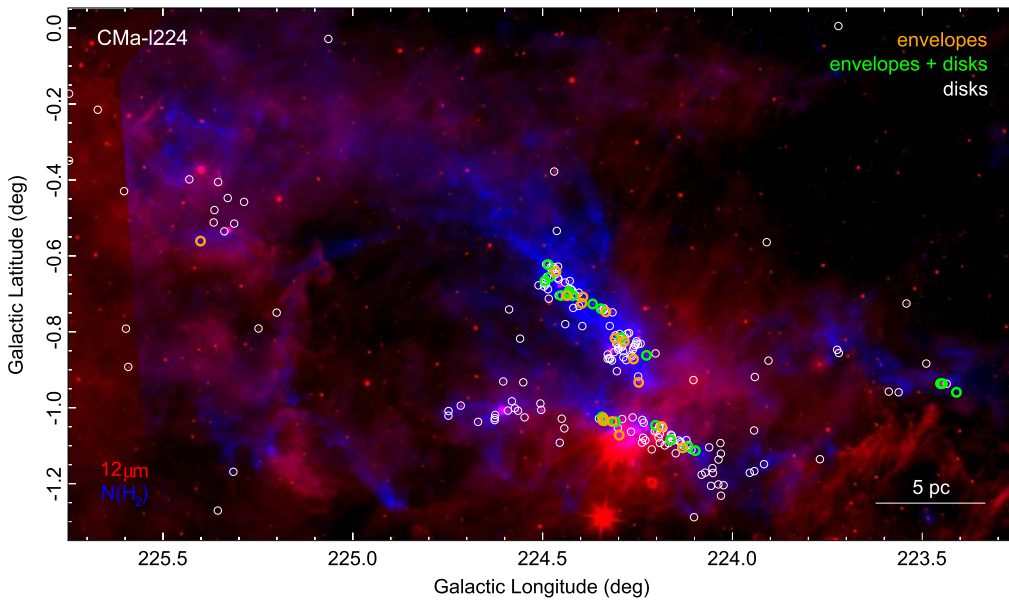


Figure 23. Two-color composite image combining the *WISE* 12 μm image (red) and the H_2 column density image (blue). The YSO candidates well fit with YSO models with the envelopes only (“envelopes”; orange circles), envelopes and disks (“envelopes + disks”; green circles), and disks only (“disks”; white circles) are concentrated in regions with the highest $N(\text{H}_2)$.

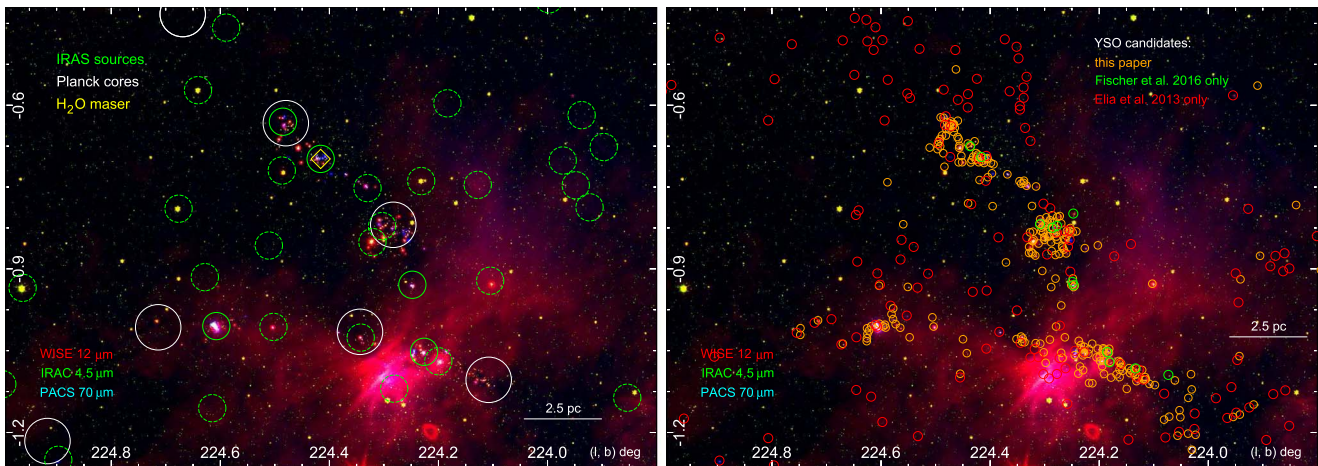


Figure 24. Left and right: three-color composite image combining the *WISE* 12 μm (red), *Spitzer*/GLIMPSE360 4.5 μm (green), and *Herschel*/Hi-GAL PACS 70 μm (blue) images. The position of the *IRAS* sources, *Planck* cold cores, and an H_2O maser (left), and YSO candidates from this paper, those from Fischer et al. (2016) only, and those from Elia et al. (2013) only are overlaid as indicated in the legends. The green solid circles in the left panel indicate *IRAS* sources associated with the CS emission. See Section 12 for details.

non-YSO contaminants. The final list of YSO candidates in CMa–l224 contains 293 sources.

We identify an additional 47 sources with the GLIMPSE360 3.6 and 4.5 μm photometry only (with no AllWISE matches or with poor-quality AllWISE photometry) that we consider “possible YSO candidates.” The vast majority of these sources are associated with high H_2 column density regions and are good targets for follow-up studies.

We determine kinematic distances to *Spitzer* sources in CMa–l224 using CO data and determine a median distance of 0.92 kpc, consistent with the distance measurement to the CMa OB1 association. We perform SED fitting with the Robitaille (2017) YSO models for sources with at least five valid flux measurements, including a 12 μm flux. Based on the SED fitting results and the PARSEC evolutionary tracks, we estimate physical parameters for 210 sources (e.g., stellar luminosities, masses, and

ages). We divide sources into three groups depending on the presence of the envelope and/or disk: “envelope-only” (16), “envelope and disk” (21), and “disk-only” (173).

The *Herschel*/SPIRE emission in CMa–l224 is highly filamentary. We compare the distribution of the YSO candidates with respect to the filaments identified by Schisano et al. (2014) based on the H_2 column density map and the filaments we identify based on the higher-resolution 250 μm image. We find that the younger population of YSO candidates, i.e., sources with “envelope-only” and “envelope and disk,” is closely associated with central regions of the filaments, while the more evolved YSO candidates (“disk-only”) are distributed more widely. This result supports the idea that stars are formed in the filaments and become more dispersed with time.

The clumpy distribution of the YSO candidates along the filaments is a very good evidence that contamination from older

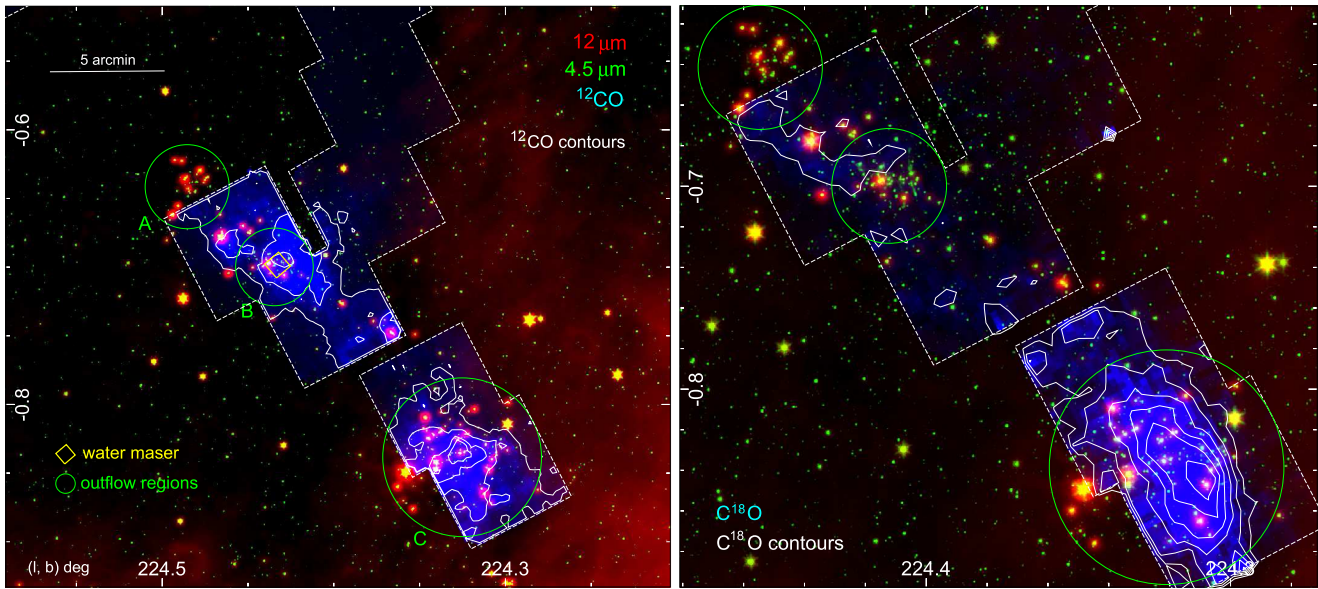


Figure 25. Three-color composite images combining the *WISE* 12 μm (red), *Spitzer*/IRAC 4.5 μm (green), and CO (blue; Olmi et al. 2016) images: ^{12}CO (left) and C^{18}O (right). The white dashed lines show the coverage of the Olmi et al. (2016) CO observations. The CO images are scaled to highlight the brightest regions. The white contours in the left panel correspond to the ^{12}CO emission at the level of (70, 80, 90, 95)% of the peak emission of $29.8 \text{ Jy beam}^{-1} \text{ km s}^{-1}$. The position of the H_2O maser is indicated with a yellow diamond. The image in the right panel is slightly zoomed in on the main filament. The white contours in the right panel correspond to the C^{18}O emission; the contour levels are (40, 50, 60, 70, 80, 90)% of the C^{18}O peak of $2.9 \text{ Jy beam}^{-1} \text{ km s}^{-1}$. The approximate positions of the regions containing sources associated with the extended 4.5 μm emission (likely outflows) are indicated with the green circles.

objects like AGB stars is very low because those would be more evenly distributed.

We compare our list of YSO candidates to the list of YSO candidates from Fischer et al. (2016) identified in Canis Major based on the *WISE* data. Eleven out of 93 Fischer et al. (2016) *WISE* YSO candidates located within the boundaries of CMA-1224 are not on our final list of YSO candidates: two were not detected by *Spitzer*, one was resolved into two *Spitzer* sources, three were removed as non-YSOs, and five did not fulfill the 2MASS-*Spitzer* (four) or [3.6][4.5]-only (one) criteria (the AllWISE photometry was not used since the distance between the AllWISE and *Spitzer* sources is larger than $1''$). We found that Group 00 of *WISE* YSO candidates from Fischer et al. (2016) corresponds to three *Spitzer* YSO candidate clusters distributed along the main filament (A, B, and C). The selection criteria based on the GLIMPSE360 data recovered more of the evolved YSO candidates (“disk-only”).

We discuss star formation in CMA-1224 in a context of the larger region—the CMA OB1 association. The main filament in CMA-1224 lies at the rim of the $\text{H}\alpha$ shell, hinting at a possible connection between the supernova event in the CMA OB1 association and star formation in the region. We discuss possible star formation scenarios: (1) the formation of the filaments in CMA-1224 as a result of the supernova explosion in the CMA OB1 association, followed by the gravitational fragmentation and the formation of prestellar cores; (2) supernova-induced star formation in the preexisting filaments; and (3) the spontaneous gravitational collapse of the filaments. All the star formation scenarios seem to be plausible; however, our results indicate that the spontaneous gravitational collapse of filaments is the most likely scenario. More evidence is needed to draw stronger conclusions.

We thank the anonymous referee for reading the paper carefully and providing useful comments. We thank Leo Girardi for providing the TRILEGAL simulation. This work

was supported by the Spitzer GLIMPSE360 project (RSA 1367334). The work of M.S. was also supported by an appointment to the NASA Postdoctoral Program at the Goddard Space Flight Center, administered by Universities Space Research Association (USRA) under contract with NASA and by NASA under award no. 80GSFC17M0002. This work was supported by the Polish National Science Center grant 2014/15/B/ST9/02111. This paper is based largely on observations made with the *Spitzer Space Telescope*, which is operated by the Jet Propulsion Laboratory, California Institute of Technology, under contract with NASA. This publication also makes use of data products from (1) the Two Micron All Sky Survey, which is a joint project of the University of Massachusetts and the Infrared Processing and Analysis Center/California Institute of Technology, funded by the National Aeronautics and Space Administration and the National Science Foundation; (2) the *Wide-field Infrared Survey Explorer*, which is a joint project of the University of California, Los Angeles, and the Jet Propulsion Laboratory/California Institute of Technology, funded by the National Aeronautics and Space Administration; (3) the *Herschel* ESA space observatory, with science instruments provided by European-led Principal Investigator consortia and with important participation from NASA; (4) *AKARI*, a JAXA project with the participation of ESA; and (5) the *Midcourse Space Experiment*; processing of the data was funded by the Ballistic Missile Defense Organization with additional support from the NASA Office of Space Science. This research has made use of the SIMBAD database, operated at CDS, Strasbourg, France.

Appendix A Catalogs from the Literature Used for the Initial Source Selection

We used the catalogs of non-YSOs, confirmed YSOs, and YSO candidates from the literature to identify regions in the

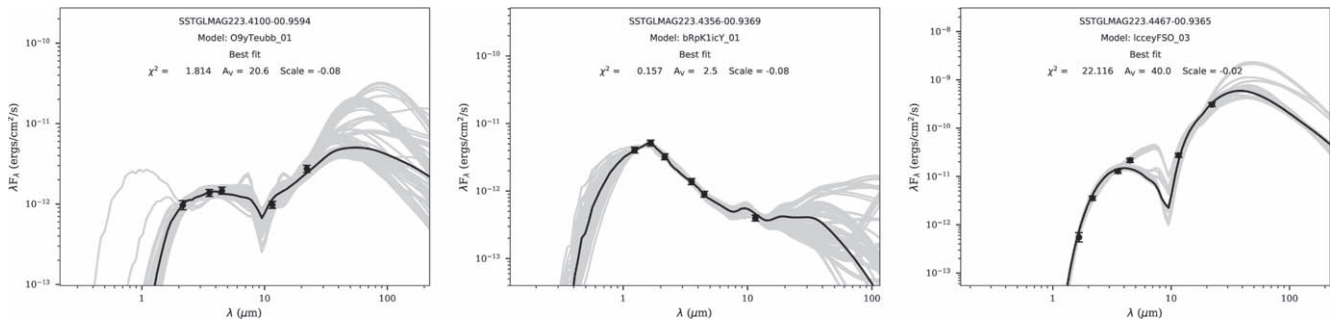


Figure 26. SEDs and the Robitaille (2017) YSO model fits for YSO candidates listed in Table 4 excluding SEDs shown in Figure 14. The symbols and lines are as in Figure 14.

(The complete figure set (204 images) is available.)

color–color and color–magnitude space where YSOs can be confused with other categories of sources. This information allowed us to select the initial list of YSO candidates that is as free of contaminants as possible. The catalogs are described below.

A.1. Non-YSOs

1. *Normal galaxies and AGNs:* AGNs and galaxies with spectroscopic redshifts from the AGN and Galaxy Evolution Survey (AGES; Kochanek et al. 2012). The AGES catalog provides spectroscopic redshifts for over 18,000 galaxies to $I = 20$ mag and ~ 5000 AGNs to $I = 22.5$ mag in the 7.7 deg^2 field. The catalog also includes photometric data for the optical (B_W , R , and I), near-IR (J , K , and K_s), and mid-IR (IRAC 3.5–8.0 μm and MIPS 24 μm) bands. The AGES survey does not provide the H -band photometry, which we use in the YSO selection process. To obtain the H -band photometry, we matched the AGES catalog to the 2MASS catalog and selected the nearest neighbors within $1''$.
2. *Planetary Nebulae (PNe):* We use the Kimeswenger (2001) catalog of southern Galactic PNe and the list of PNe identified in Urquhart et al. (2009). The Kimeswenger (2001) catalog includes ~ 1000 ($>99\%$) sources from the Strasbourg-ESO Catalog of Galactic Planetary Nebulae (and the first supplement to this catalog), but it provides more accurate optical coordinates than the original catalog. Urquhart et al. (2009) identified >50 PNe in the northern hemisphere as part of The Red *MSX* Source (RMS) survey, which is a multiwavelength observational program that aims to identify a large sample of massive YSOs in the Galaxy. Urquhart et al. (2009) identified PNe based on a combination of 6 cm radio, CO, and near- to far-IR data and removed them from the YSO list. We used the General Catalog Query Engine in the NASA/IRSA Infrared Science Archive to search for the mid-IR counterparts to the PNe from Kimeswenger (2001) and Urquhart et al. (2009) in the *Spitzer* GLIMPSE surveys¹⁹: GLIMPSE I, GLIMPSE II, GLIMPSE 3D, GLIMPSE360, and Deep GLIMPSE (Benjamin et al. 2003). We selected the nearest matches in the IRAC Archive within $1''$. The matching provided us with the 2MASS and IRAC photometry for ~ 120 PNe.

3. *Evolved stars:* The sample of 54 Galactic evolved stars comes from Reiter et al. (2015) and includes 48 AGB stars (22 O-rich, 19 C-rich, and 7 S-type) and 6 supergiants. The Reiter et al. (2015) catalog provides the 2MASS and IRAC photometry. As for PNe, we searched the AllWISE catalog for the closest matches to evolved stars within $1''$. The resulting sample of evolved stars with AllWISE photometry contains 45 sources. For all of these sources, the $w1$ and $w2$ magnitudes are upper limits; thus, this sample of evolved stars is not included in CCDs and CMDs that use these bands.

A.2. Known Galactic YSOs and YSO Candidates

1. *Photometrically selected YSOs:* We make use of the Dunham et al. (2015) catalog of YSOs identified in 18 molecular clouds covered by the *Spitzer* Legacy Surveys “From Molecular Cores to Planet-Forming Disks” (c2d; Evans et al. 2003) and “Gould’s Belt: Star Formation in the Solar Neighborhood” (Allen & *Spitzer* Gould Belt Legacy Team 2007). Using the YSO selection techniques developed for these surveys combined with the visual inspection, Dunham et al. (2015) identified 2966 YSO candidates. Out of 2966, 326 (11%), 210 (7%), 1248 (42%), and 1182 (40%) are classified as Class 0+I, flat-spectrum, Class II, and Class III, respectively. We only include sources that are not flagged as potential AGB star contaminants.
2. *YSOs observed spectroscopically:* We use the catalog of ~ 1390 YSOs in L1641 from Fang et al. (2013). The YSOs were identified using the multiwavelength photometry (including *Spitzer*, *WISE*, 2MASS, and *XMM*) and optical spectroscopy. We selected sources that either were observed spectroscopically or are associated with X-ray emission (an accretion tracer). About 72% of sources fulfill these criteria (62% observed spectroscopically): 38, 323, 503, 66, and 66 YSOs are classified as Stage I, Stage II, Stage II, flat, and transition disks (TDs), respectively.

Appendix B Spectral Energy Distribution and YSO Model Fits for YSO Candidates

We present SEDs and the Robitaille (2017) YSO model fits for YSO candidates listed in Table 4 (see Figure 26). The

¹⁹ A zoomable web browser showing the GLIMPSE surveys can be found at www.alienearts.org/glimpse, and at www.spitzer.caltech.edu/glimpse360 for the GLIMPSE360 survey.

symbols and lines are as in Figure 14. The YSO fitting is described in Section 6.

Appendix C

A Comparison between the YSO Candidate Lists

We matched the final list of YSO candidates to the Fischer et al. (2016) catalog using the AllWISE designations. Out of the 93 YSO candidates from Fischer et al. (2016) located in CMA-1224, 20 AllWISE sources are not in our final list of YSO candidates.

Two out of 20 *WISE* sources were not detected by *Spitzer* (J070724.82–094712.0, J070927.40–102921.0), and one source was resolved into multiple *Spitzer* sources (J070810.47–102720.3); one of these sources is in the GLIMPSE360 catalog with a position offset $>3''$ from the *WISE* position.

For 12 *WISE* sources selected as YSO candidates in Fischer et al. (2016), the distance between the *Spitzer* and AllWISE catalog source was larger than $1''$, and the AllWISE match was removed (J070613.51–095837.9, J070801.11–102427.5, J070818.24–102933.9, J070822.75–102916.3, J070856.28–102910.4, J070923.27–102747.4, J070923.42–102818.8, J070924.77–102534.0, J071012.84–103213.0, J071023.74–103327.1, J071024.84–103247.7, J071306.61–111803.8).

1. After removing the AllWISE photometry, 5 out of 12 *Spitzer* sources had only 3.6 and 4.5 μm photometry left; four of these sources are included in our [3.6][4.5]-only source list of “possible YSO candidates” (J070822.75–102916.3, J070923.42–102818.8, J071306.61–111803.8, J070613.51–095837.9). One source (J070856.28–102910.4) does not have the GLIMPSE360 Catalog counterpart and was removed from the list.
2. Four out of 12 sources did not fulfill the 2MASS–*Spitzer* YSO selection criteria and were removed from the list (J070801.11–102427.5, J070924.77–102534.0, J070923.27–102747.4, J071012.84–103213.0).
3. One source was well fit with the stellar photosphere model and removed (J070818.24–102933.9).
4. Two sources are on our final YSO candidate list (J071024.84–103247.7, J071023.74–103327.1).

For five *WISE* sources selected as YSO candidates in Fischer et al. (2016), the distance between the *Spitzer* and AllWISE catalog source was less than $1''$ and a combined *Spitzer* and AllWISE photometry was used in the analysis.

1. Two out of five sources were removed as background galaxy candidates (J070857.81–102906.5, J071006.22–103140.2).
2. Three sources are on the final list of YSO candidates, but the AllWISE matches/photometry were removed based on the `ext_flg` criterion (J071222.96–111625.1, J070920.64–102817.4, J070925.85–102907.7).

In summary, out of 20 Fischer et al. (2016) YSO candidates not matched to our final list of YSO candidates using AllWISE designation, 5 are classified as YSO candidates based on the 2MASS and *Spitzer* photometry only, and 4 are on the [3.6][4.5]-only list of possible YSO candidates. Seven GLIMPSE360 sources that were initially matched to AllWISE sources were removed from the list based on the 2MASS and GLIMPSE360 photometry. One source that became an [3.6][4.5]-only source after removing the AllWISE photometry in the initial selection of YSO candidates was removed owing to

the lack of the GLIMPSE360 Catalog counterpart. Three YSO candidates from Fischer et al. (2016) do not have a clear *Spitzer* counterpart.

ORCID iDs

Marta Sewilo  <https://orcid.org/0000-0003-2248-6032>
 Thomas P. Robitaille  <https://orcid.org/0000-0002-8642-1329>
 Davide Elia  <https://orcid.org/0000-0002-9120-5890>
 Remy Indebetouw  <https://orcid.org/0000-0002-4663-6827>
 Eugenio Schisano  <https://orcid.org/0000-0003-1560-3958>
 Ryszard Szczerba  <https://orcid.org/0000-0003-2886-4460>
 Agata Karska  <https://orcid.org/0000-0001-8913-925X>
 Jennifer Wiseman  <https://orcid.org/0000-0002-1143-6710>
 Brian Babler  <https://orcid.org/0000-0002-6984-5752>
 Martha L. Boyer  <https://orcid.org/0000-0003-4850-9589>
 William J. Fischer  <https://orcid.org/0000-0002-3747-2496>
 Luca Olmi  <https://orcid.org/0000-0002-1162-7947>
 Deborah Padgett  <https://orcid.org/0000-0001-5334-5107>

References

- Allen, L. & Spitzer Gould Belt Legacy Team 2007, *BAAS*, **39**, 881
 Ambartsumian, V. A. 1949, *DokAN*, **68**, 21
 André, P. 2017, *CRGeo*, **349**, 187
 André, P., Di Francesco, J., Ward-Thompson, D., et al. 2014, in *Protostars and Planets VI*, ed. H. Beuther et al. (Tucson, AZ: Univ. Arizona Press), 27
 Audard, M., Ábrahám, P., Dunham, M. M., et al. 2014, in *Protostars and Planets VI*, ed. H. Beuther et al. (Tucson, AZ: Univ. Arizona Press), 387
 Bailer, D. S., Rood, R. T., Bania, T. M., & Anderson, L. D. 2011, *ApJ*, **738**, 27
 Beerer, I. M., Koenig, X. P., Hora, J. L., et al. 2010, *ApJ*, **720**, 679
 Benedettini, M., Schisano, E., Pezzuto, S., et al. 2015, *MNRAS*, **453**, 2036
 Benjamin, R. A., Churchwell, E., Babler, B. L., et al. 2003, *PASP*, **115**, 953
 Bloemen, J. B. G. M., Bennett, K., Bignami, G. F., et al. 1984, *A&A*, **135**, 12
 Bohlin, R. C., Savage, B. D., & Drake, J. F. 1978, *ApJ*, **224**, 132
 Bresnahan, D., Ward-Thompson, D., Kirk, J. M., et al. 2018, *A&A*, **615**, A125
 Bressan, A., Marigo, P., Girardi, L., et al. 2012, *MNRAS*, **427**, 127
 Bronfman, L., Nyman, L.-A., & May, J. 1996, *A&AS*, **115**, 81
 Brunthaler, A., Reid, M. J., Menten, K. M., et al. 2011, *AN*, **332**, 461
 Castelli, F., & Kurucz, R. L. 2004, arXiv:astro-ph/0405087
 Chen, C.-Y., & Ostriker, E. C. 2014, *ApJ*, **785**, 69
 Chen, Y., Bressan, A., Girardi, L., et al. 2015, *MNRAS*, **452**, 1068
 Chen, Y., Girardi, L., Bressan, A., et al. 2014, *MNRAS*, **444**, 2525
 Clariá, J. J. 1974a, *AJ*, **79**, 1022
 Clariá, J. J. 1974b, *A&A*, **37**, 229
 Comerón, F., Torra, J., & Gomez, A. E. 1998, *A&A*, **330**, 975
 Cyganowski, C. J., Brogan, C. L., Hunter, T. R., Churchwell, E., & Zhang, Q. 2011, *ApJ*, **729**, 124
 Cyganowski, C. J., Koda, J., Rosolowsky, E., et al. 2013, *ApJ*, **764**, 61
 Cyganowski, C. J., Whitney, B. A., Holden, E., et al. 2008, *AJ*, **136**, 2391
 Dias, W. S., Alessi, B. S., Moitinho, A., & Lépine, J. R. D. 2002, *A&A*, **389**, 871
 Dunham, M. M., Allen, L. E., Evans, N. J., II, et al. 2015, *ApJS*, **220**, 11
 Egan, M. P., Price, S. D., Kraemer, K. E., et al. 2003, *yCat*, **5114**, 0
 Elia, D., Molinari, S., Fukui, Y., et al. 2013, *ApJ*, **772**, 45
 Evans, N. J., II, Allen, L. E., Blake, G. A., et al. 2003, *PASP*, **115**, 965
 Fang, M., Kim, J. S., van Boekel, R., et al. 2013, *ApJS*, **207**, 5
 Fazio, G. G., Hora, J. L., Allen, L. E., et al. 2004, *ApJS*, **154**, 10
 Fischer, W. J., Padgett, D. L., Stapelfeldt, K. L., & Sewilo, M. 2016, *ApJ*, **827**, 96
 Fitzgerald, M. P., Harris, G. L., & Reed, B. C. 1990, *PASP*, **102**, 865
 Flaherty, K. M., Pipher, J. L., Megeath, S. T., et al. 2007, *ApJ*, **663**, 1069
 Foster, J. B., Mandel, K. S., Pineda, J. E., et al. 2013, *MNRAS*, **428**, 1606
 Frémat, Y., Neiner, C., Hubert, A.-M., et al. 2006, *A&A*, **451**, 1053
 Gaustad, J. E., McCullough, P. R., Rosing, W., & Van Buren, D. 2001, *PASP*, **113**, 1326
 Girardi, L., Groenewegen, M. A. T., Hatziminaoglou, E., & da Costa, L. 2005, *A&A*, **436**, 895
 Gregorio-Hetem, J. 2008, in *Handbook of Star Forming Regions II*, ed. B. Reipurth (Tucson, AZ: Univ. Arizona Press), 1
 Gregorio-Hetem, J., Montmerle, T., Rodrigues, C. V., et al. 2009, *A&A*, **506**, 711
 Griffin, M. J., Abergel, A., Abreu, A., et al. 2010, *A&A*, **518**, L3

- Gutermuth, R. A., Megeath, S. T., Myers, P. C., et al. 2009, *ApJS*, **184**, 18
- Harju, J., Lehtinen, K., Booth, R. S., & Zinchenko, I. 1998, *A&AS*, **132**, 211
- Hartmann, L. 2002, *ApJ*, **578**, 914
- He, J. H., Takahashi, S., & Chen, X. 2012, *ApJS*, **202**, 1
- Herbst, W., & Assousa, G. E. 1977, *ApJ*, **217**, 473
- Herbst, W., Racine, R., & Warner, J. W. 1978, *ApJ*, **223**, 471
- Inutsuka, S.-i., Inoue, T., Iwasaki, K., & Hosokawa, T. 2015, *A&A*, **580**, A49
- Ishihara, D., Onaka, T., Kataza, H., et al. 2010, *A&A*, **514**, A1
- Jarrett, T. H., Cohen, M., Masci, F., et al. 2011, *ApJ*, **735**, 112
- Kaltcheva, N. T., & Hilditch, R. W. 2000, *MNRAS*, **312**, 753
- Kataza, H., Alfageme, C., & Cassatella, A. 2010, AKARI/IRC All-Sky Point Source Catalog, Release Note v1.0, (Sagamihara: AKARI), http://www.ir.isas.jaxa.jp/AKARI/Observation/PSC/Public/RN/AKARI-IRC_PSC_V1_RN.pdf
- Kauffmann, J., & Pillai, T. 2010, *ApJL*, **723**, L7
- Kharchenko, N. V., Piskunov, A. E., Schilbach, E., Röser, S., & Scholz, R.-D. 2013, *A&A*, **558**, A53
- Kim, B. G., Kawamura, A., Yonekura, Y., & Fukui, Y. 2004, *PASJ*, **56**, 313
- Kimeswenger, S. 2001, *RMxAA*, **37**, 115
- Kirk, H., Myers, P. C., Bourke, T. L., et al. 2013, *ApJ*, **766**, 115
- Koch, E. W., & Rosolowsky, E. W. 2015, *MNRAS*, **452**, 3435
- Kochanek, C. S., Eisenstein, D. J., Cool, R. J., et al. 2012, *ApJS*, **200**, 8
- Koenig, X. P., & Leisawitz, D. T. 2014, *ApJ*, **791**, 131
- Könyves, V., André, P., Men'shchikov, A., et al. 2015, *A&A*, **584**, A91
- Lim, B., Sung, H. S., Karimov, R., & Ibrahimov, M. 2011, *JKAS*, **44**, 39
- Lombardi, M., Alves, J., & Lada, C. J. 2011, *A&A*, **535**, A16
- Magakian, T. Y. 2003, *A&A*, **399**, 141
- Mainzer, A., Bauer, J., Grav, T., et al. 2011, *ApJ*, **731**, 53
- Marigo, P., Bressan, A., Nanni, A., Girardi, L., & Pumo, M. L. 2013, *MNRAS*, **434**, 488
- Meade, M. R., Whitney, B., & Babler, B. 2014, GLIMPSE360 Data Description —GLIMPSE360: Completing the Spitzer Galactic Plane Survey, (Pasadena, CA: IPAC), http://irsa.ipac.caltech.edu/data/SPITZER/GLIMPSE/doc/glimpse360_dataproduct_v1.5.pdf
- Megeath, S. T., Gutermuth, R., Muzerolle, J., et al. 2012, *AJ*, **144**, 192
- Miller, A. A., Hillenbrand, L. A., Bilgi, P., et al. 2015, *ATel*, **7428**
- Mizuno, A., & Fukui, Y. 2004, in ASP Conf. Ser. 317, *Milky Way Surveys: The Structure and Evolution of our Galaxy*, ed. D. Clemens, R. Shah, & T. Brainerd (San Francisco, CA: ASP), 59
- Moitinho, A., Vázquez, R. A., Carraro, G., et al. 2006, *MNRAS*, **368**, L77
- Molinari, S., Schisano, E., Elia, D., et al. 2016, *A&A*, **591**, A149
- Molinari, S., Swinyard, B., Bally, J., et al. 2010, *PASP*, **122**, 314
- Murakami, H., Baba, H., Barthel, P., et al. 2007, *PASJ*, **59**, 369
- Nakano, M., Yoshida, S., & Kogure, T. 1984, *PASJ*, **36**, 517
- Navarete, F., Damini, A., Barbosa, C. L., & Blum, R. D. 2015, *MNRAS*, **450**, 4364
- Olmi, L., Cunningham, M., Elia, D., & Jones, P. 2016, *A&A*, **594**, A58
- Onaka, T., Matsuhara, H., Wada, T., et al. 2007, *PASJ*, **59**, 401
- Palmeirim, P., André, P., Kirk, J., et al. 2013, *A&A*, **550**, A38
- Paturel, G., Petit, C., Prugniel, P., et al. 2003, *A&A*, **412**, 45
- Pecaut, M. J., & Mamajek, E. E. 2013, *ApJS*, **208**, 9
- Petrov, L., Kovalev, Y. Y., Fomalont, E. B., & Gordon, D. 2011, *AJ*, **142**, 35
- Pilbratt, G. L., Riedinger, J. R., Passvogel, T., et al. 2010, *A&A*, **518**, L1
- Planck Collaboration, Ade, P. A. R., Aghanim, N., et al. 2016, *A&A*, **594**, A28
- Poglitsch, A., Waelkens, C., Geis, N., et al. 2010, *A&A*, **518**, L2
- Povich, M. S., Smith, N., Majewski, S. R., et al. 2011, *ApJS*, **194**, 14
- Reiter, M., Marengo, M., Hora, J. L., & Fazio, G. G. 2015, *MNRAS*, **447**, 3909
- Reynolds, R. J., & Ogdén, P. M. 1978, *ApJ*, **224**, 94
- Robitaille, T. P. 2017, *A&A*, **600**, A11
- Robitaille, T. P., Whitney, B. A., Indebetouw, R., & Wood, K. 2007, *ApJS*, **169**, 328
- Robitaille, T. P., Whitney, B. A., Indebetouw, R., Wood, K., & Denzmore, P. 2006, *ApJS*, **167**, 256
- Rosolowsky, E., & Leroy, A. 2006, *PASP*, **118**, 590
- Rosolowsky, E., & Leroy, A. 2011, CPROPS: Bias-free Measurement of Giant Molecular Cloud Properties, Astrophysics Source Code Library, [ascl:1102.012](https://ui.adsabs.org/abs/2011ascl...1102012R)
- Ruprecht, J. 1966, *IAU Trans*, **12B**, 348
- Rybakin, B., & Goryachev, V. 2018, *CF*, **173**, 189
- Salji, C. J., Richer, J. S., Buckle, J. V., et al. 2015, *MNRAS*, **449**, 1782
- Schisano, E., Molinari, S., Elia, D., et al. 2018, *MNRAS*, submitted
- Schisano, E., Rygl, K. L. J., Molinari, S., et al. 2014, *ApJ*, **791**, 27
- Sharpless, S. 1959, *ApJS*, **4**, 257
- Shevchenko, V. S., Ezhkova, O. V., Ibrahimov, M. A., van den Ancker, M. E., & Tjin A Dje, H. R. E. 1999, *MNRAS*, **310**, 210
- Skrutskie, M. F., Cutri, R. M., Stiening, R., et al. 2006, *AJ*, **131**, 1163
- Tanabé, T., Sakon, I., Cohen, M., et al. 2008, *PASJ*, **60**, 375
- Tang, J., Bressan, A., Rosenfield, P., et al. 2014, *MNRAS*, **445**, 4287
- Tapia, M., Persi, P., Bohigas, J., & Ferrari-Toniolo, M. 1997, *AJ*, **113**, 1769
- Urquhart, J. S., Hoare, M. G., Purcell, C. R., et al. 2009, *A&A*, **501**, 539
- Valdettaro, R., Palla, F., Brand, J., et al. 2001, *A&A*, **368**, 845
- van den Bergh, S. 1966, *AJ*, **71**, 990
- Vollmer, B., Gassmann, B., Derrière, S., et al. 2010, *A&A*, **511**, A53
- Weingartner, J. C., & Draine, B. T. 2001, *ApJ*, **548**, 296
- Werner, M. W., Roellig, T. L., Low, F. J., et al. 2004, *ApJS*, **154**, 1
- Williams, J. P., de Geus, E. J., & Blitz, L. 1994, *ApJ*, **428**, 693
- Willis, S., Marengo, M., Allen, L., et al. 2013, *ApJ*, **778**, 96
- Winston, E., Megeath, S. T., Wolk, S. J., et al. 2007, *ApJ*, **669**, 493
- Wouterloot, J. G. A., & Brand, J. 1989, *A&AS*, **80**, 149
- Wright, A. E., Griffith, M. R., Hunt, A. J., et al. 1996, *ApJS*, **103**, 145
- Wright, E. L., Eisenhardt, P. R. M., Mainzer, A. K., et al. 2010, *AJ*, **140**, 1868
- Zahorecz, S., Jimenez-Serra, I., Wang, K., et al. 2016, *A&A*, **591**, A105